Fuel 381 (2025) 133386

Contents lists available at ScienceDirect

Fuel

journal homepage: www.elsevier.com/locate/fuel

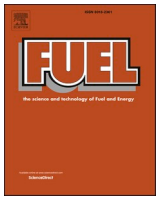

Full Length Article

A platinum-coated staggered reactor to intensify lean hydrogen/air combustion: A large eddy simulation study

Md Nur Alam Mondal [a], Nader Karimi [a,c], S. David Jackson [b], Manosh C. Paul [a,*]

[a] James Watt School of Engineering, University of Glasgow, Glasgow G12 8QQ, United Kingdom
[b] School of Chemistry, University of Glasgow, Glasgow G12 8QQ, United Kingdom
[c] School of Engineering and Materials Science, Queen Mary University of London, London E14 NS, United Kingdom

ARTICLE INFO

Keywords:
Turbulent catalytic combustion
Platinum catalyst
Large eddy simulation
Process intensification

ABSTRACT

Catalytic-aided combustion has been proven effective for premixed hydrogen/air mixtures, particularly under lean to ultra-lean conditions. However, minimising the required catalyst sets a significant challenge because noble metals with high catalytic activity are rare and expensive. Therefore, this study aims to intensify the catalytic combustion process by investigating a non-planar reactor comprising an array of platinum-coated half- and full-cylinders through large eddy simulation. A premixed mixture with a fuel-lean equivalence ratio of 0.15 and an incoming Reynolds number of 3500 based on hydraulic diameter is used. For comparison, a planar reactor without cylinders is also studied under the same operating conditions and with the same amount of platinum-coated surface area. The simulation employs the turbulent kinetic energy sub-grid model and the eddy dissipation concept to model the turbulent catalytic reacting flow. The discrete ordinate model is used to account for radiation heat transfer in the catalytic process. Numerical simulations are validated against experimental results prior to analysis. The findings indicate that the placement of cylinders along the reactor length enhances convective mass transfer and intensifies catalytic combustion, resulting in effective combustion over a smaller catalytic surface. Compared to planar models, non-planar reactors demonstrate a much better H_2 conversion efficiency throughout the reactor length, saving nearly 62.5 % of the catalyst.

1. Introduction

Catalytic combustion of hydrogen is a modern technology and is being implemented in various reactor applications [1–3]. Among these applications, catalytic combustion of premixed mixtures has been found to be effective in reducing NO_x emissions [2,4] and in enhancing syngas combustion [5,6]. In previous studies [7–10], efforts have been made to develop planar reactors with catalyst-coated inner walls. The fuel conversion inside the reactor is governed by either homogeneous combustion or heterogeneous combustion, or both based on inflow and reactor wall thermal condition [11]. The coexistence of homogeneous and heterogeneous combustion is advantageous due to reduced reliance on catalysts [12]. However, in reactors operated with lean mixtures, a significant amount of catalyst is required, with fuel conversion predominantly occurring through heterogeneous combustion [11]. This can result in superadiabatic surface temperatures at the catalytic walls [13,14]. In many cases, localised hotspots (where the local wall temperature exceeds the average temperature) can form if the support material is unable to dissipate heat effectively [15,16]. Although some recent studies [17–19] have explored catalyst and reactor designs aimed at minimising elevated wall temperatures and enhancing combustion stability, further research is needed to evaluate their effectiveness under diverse operating conditions. Reducing the catalyst requirement for complete combustion presents a significant challenge due to the high cost of rare metals used as catalysts. Additionally, accommodating sufficient catalyst in planar reactors necessitates increased reactor length, leading to a more robust but less economical and practical design [11]. Moreover, in planar reactors, surface reaction rates often reach a plateau due to limited mass transfer of fuel species toward the catalytic walls [14,20]. Therefore, catalytic reactors with the enhanced mass transfer of fuel species to reactive walls, compact designs and optimal catalysts are of prime interest for their wide-ranging application [13,21]. To progress on catalytic reactors, the multidimensional modelling of optimal catalytic coating is necessary for reactor design.

One application of catalytic reactors is honeycomb structures, which consist of multitube catalyst-coated channels with a hydraulic diameter in the millimetre range. To enhance mass transfer with an optimal

* Corresponding author.
E-mail address: Manosh.Paul@glasgow.ac.uk (M.C. Paul).

https://doi.org/10.1016/j.fuel.2024.133386
Received 27 June 2024; Received in revised form 2 October 2024; Accepted 5 October 2024
Available online 9 October 2024

Nomenclature

D	cylinder diameter (m)
H	enthalpy (kj/kg)
H	reactor height (m)
k	turbulent kinetic energy (m^2/s^2)
M	molecular weight (kg/kmol)
N_s	total of number of surface species (−)
N_g	total number of gas species (−)
p	pressure (N/m^2)
P	cylinder pitch (m)
Pr	Prandtl number (−)
q	heat flux (W/m^2)
Re	Reynolds number (−)
$\dot{s}$	molar production rate (mol/m^2s)
Sc	Schmidt number (−)
T	temperature (K)
u_t	friction velocity (m/s)
$\dot{w}$	reaction rate of gas species (kg/m^3s)
y	transverse coordinate (m)
X	mole fraction (−)
Y	mass fraction (−)
x	streamwise coordinate (m)
z	spanwise coordinate (m)

Greek symbols

ρ	density (kg/m^3)
μ	dynamic viscosity (kg/ms)
φ	equivalence ratio (−)
λ	thermal conductivity (W/mK)
Γ	surface site density (mol/cm^2)
Θ	surface coverage (−)
δ	wall thickness (m)

Subscripts

avg	average
g	fluid
in	inlet
m	mean
rms	root mean square
s	solid
w	wall surface

Superscripts

−	filtered variable

Acronyms

DNS	Direct Numerical Simulations
LES	Large Eddy Simulation
RANS	Reynolds Averaging Navier Stokes
SGS	Subgrid-scale

catalyst in honeycomb channels, a novel reactor design has been adopted with appropriate geometric modifications [22]. Carrying out experimental work in such reactors is exceedingly challenging, particularly in the precise measurement of species concentration and temperature near the catalytic wall [23,24]. Consequently, numerical simulation is the preferred approach for investigating catalytic processes. In this context, the proper selection of turbulence models is essential for accurately simulating the complex turbulent flows inside the reactor, because the turbulent effect becomes weaker when it involves the catalytic reaction with the flows [23]. Moreover, the turbulent flow significantly affects the catalytic activity as the mass transport toward or away from the catalytic surface increases with turbulence [23,25]. Therefore, a reliable numerical model is essential to capture the near-wall turbulence and the catalytic process. Reynolds Averaging Navier Stokes (RANS) models are widely used [23,26,27] for modelling turbulent catalytic reacting flows. However, RANS models struggle to capture the effects of separated flow in reacting flows with non-planar surfaces. In this regard, Direct Numerical Simulations (DNS) are the best numerical models to capture near-wall turbulence, but this is computationally expensive and difficult to model complex combustion dynamics with catalytic reactions. Though some studies using DNS [28–30] for turbulent catalytic combustion systems have been reported in the literature, the reacting DNS is challenging for spatially developing flows, particularly for the reactor configuration discussed in the present study. The Large Eddy Simulations (LES) are, therefore, practical options to simulate most of the turbulent reacting flows [31]. Though the LES is limited to modelling large-scale turbulence, this is still useful for predicting realistic combustion processes [32–34]. Nonetheless, currently, there is a noticeable research gap in the application of LES to catalytic combustion processes. This work aims to address that gap by evaluating the effectiveness of LES in modelling catalytic combustion systems, highlighting its potential to enhance our understanding and prediction of these complex processes.

Previous studies [23,28–30] investigated the catalytic turbulent reacting flow in a channel or planar reactor, with an inflow Reynolds number of up to 30,000. The high Reynolds number was considered to understand the effect of flow laminarisation, which occurs within the boundary layer and near the catalytic surface due to increased viscosity from heating by the catalytic surfaces. As reported in earlier studies [23], the laminarisation effect is expected to be more pronounced at low Reynolds number turbulent flows. However, the impact of flow laminarisation on catalytic reactors with non-planar surfaces is not yet known and requires further investigation. Therefore, comparatively a low turbulent Reynolds number of 3500 (based on the hydraulic diameter and the mean inlet velocity) is chosen to simulate the turbulent catalytic combustion with detailed chemistry (both heterogeneous and homogeneous). Simulations are performed on both planar and modified non-planar catalytic reactors at fuel lean H_2/air mixtures (equivalence ratios $\varphi = 0.15$).

The present work aims to intensify catalytic hydrogen/air combustion while reducing the reliance on expensive platinum catalysts. The innovation lies in the use of catalyst-coated staggered cylinders within the reactor to significantly improve the catalytic process. Furthermore, numerical simulations of turbulent catalytic combustion using LES are still limited, especially for reactors with cylindrical geometries as examined in this study, due to the challenges in accurately capturing the impact of reactor geometry on combustion dynamics. This study introduces a crucial design modification to catalytic reactors, paving the way for further advancements in catalytic combustion.

This article is organised in the following way: Section 2 explains the numerical methodology and presents validated results. Then, in Section 3, the discussion of the turbulent flow characteristics for both planar and non-planar configurations is presented, comparing the velocity, temperature and species distribution inside the reactor. Finally, the article concludes with a summary of the findings in Section 4.

2. Numerical approach

The catalytic reactor configuration, governing equations and numerical settings required to simulate turbulent catalytic reacting flow are discussed below.

2.1. Catalytic reactor configurations

The study investigates turbulent catalytic reacting flow in two reactor configurations. The first configuration is a planar one similar to the flow between parallel plates where a portion of inner surfaces is catalyst coated. It is noted that most previous studies on turbulent catalytic combustion have been focused on this configuration [29,30].The second configuration is the non-planar reactor that represents the flow through an array of half- and full −cylindrical rods where a portion of cylindrical surfaces are coated with catalysts. Such configuration has not been subjected to any study in the past. The computational domain is illustrated in Fig. 1. The catalytic reactors are 11.67H in length and 1.5H in width, where H is the distance between the parallel plates and δ is the thickness of the plate. The cylinder pitch is denoted as P and its value of 2d is considered in the present case. The catalytic surfaces are highlighted in red in both configurations. The inner surfaces of $1.75 \leq x/H \leq 8.82$ are coated with platinum in the planar reactor. The non-planar reactor contains six half cylinders attached to each reactor wall, and six full cylinders placed between the half cylinders along the centreline of the reactor. The centre of the first full cylinder is placed at a distance of 4d from the inlet. The distance between the centres of the half and full cylinders is d.

The key design parameters for a non-planar reactor include cylinder size, aspect ratio, and spacing between the cylinders, all of which can significantly influence flow dynamics and catalytic performance. While the impact of variations in these parameters is not explored in the current study, the catalytic surfaces in the non-planar reactor are chosen where the mass and heat transfers are more effective. For this reason, only cylindrical surfaces are coated with platinum, except a quarter of the back uncoated. This is because flow separation occurs downstream of both half and full cylinders [22,35] which significantly affects the convective mass and heat transfer in that particular region. The total catalytic surface area for both configurations is kept the same for comparison. Table 1 provides the other necessary information of geometric and operational parameters. The catalytic reactor operates by introducing a mixture of hydrogen and air into the inlet. The reaction is initiated on the catalytic surfaces and the resulting products are then released through the outlet. A Reynolds number (Re) of 3500 is used in both the catalytic reactors, based on the bulk velocity at the inlet and the hydraulic diameter. The inflow conditions such as flow velocity, temperature, and species mass fraction are kept uniform with a turbulence intensity of 5.7 % estimated based on the flow Reynolds number. At the outlet, all the variables have a zero-gradient condition except for the pressure which remains at an atmospheric level. The gas–solid boundary conditions at the interface of the reactor are as follows:

- The flow velocity components, $U = 0$, $V = 0$, and $W = 0$ as the no-slip conditions.
- The gas phase species boundary conditions at the catalytic surface are specified by $n_i[\rho Y_{g,j}\,(V_{g,j} + u_i)]_w = M_{g,j}\dot{s}_{g,j}$, $j = 1, 2, 3,\ldots, N_g$, where V_g, M_g, and $\dot{s}_g$ are the diffusion velocity, molecular weight and catalytic molar production rate of gas species, respectively. n_i is the unit outward-pointing component normal to a surface, and u_i is the Stefan velocity. This Stephan velocity, arising from the net mass flux between the surface and the gas in catalytic process, is significant in transient formulations [36] and given by $n_i u_i = (1/\rho)\sum_{j=1}^{N_g} M_{g,j}\dot{s}_{g,j}$ [37]. However, for statistically steady-state solutions, the temporal fluctuations around the mean values do not generate significant Stefan velocities. Consequently, although u is nonzero, it is negligible in the present case.
- The thermal boundary conditions at the fluid and solid interface are set coupled.
- The outer walls and the vertical facets of the plates are considered to be adiabatic.
- The spanwise z-direction is subject to be a periodic boundary condition.
- The thermal conductivity of steel ($\lambda_s = 16.27\ \mathrm{Wm^{-1}K^{-1}}$) is considered for heat conduction in solids.
- The process of thermal radiation from the hot catalytic surfaces towards the inlet and outlet is simulated using the discrete ordinates (DO) model. This model is uncoupled, and 10 iterations are set for energy per radiation iteration.
- The radiation heat transfer is considered at the inlet and outlet enclosures with an internal emissivity of 1.0 at the boundary temperature.

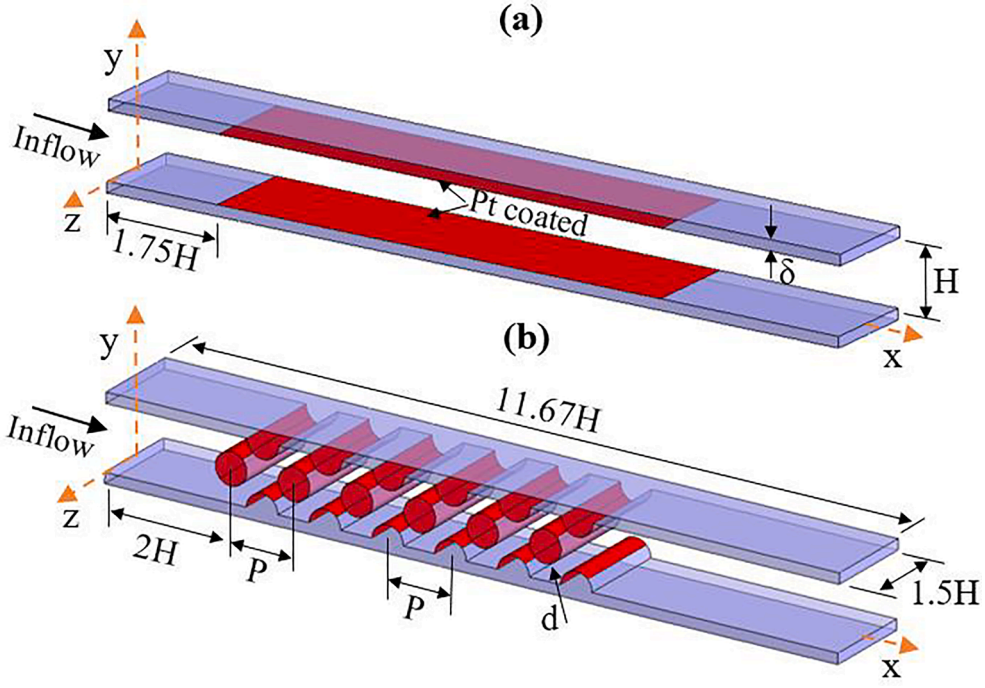

Fig. 1. Schematics of the (a) planar and (b) non-planar reactors.

Table 1
Simulated cases.

Case	**C1.** Planar (Reacting)	**C2.** Non-Planar (Non-Reacting)	**C3.** Planar (Non–/Reacting)		**C4.** Non-Planar (Reacting)	
Dimension	$35.7H \times H \times 1.5H$; $H = 7$ mm	$10.5H \times H \times 1.5H$; $P = 1.73H$; $D = 0.59H$; $H = 85.3$ mm	$11H \times H \times 1.5H$; $H = 3$ mm; $\delta = 0.5$ mm		$11H \times H \times 1.5H$; $P=H$; $D=H/2$; $H = 3$ mm; $\delta = 0.5$ mm	
Grid	C1	C2	C3-M1	C3-M2	C4-M1	C4-M2
Fluid domain	3,136,000	7,224,000	756,000	1,225,000	1,477,400	3,826,900
Solid domain	–	–	378,000	525,000	1,246,520	3,520,860
Inflow conditions	$T_{in} = 300$ K, $\varphi = 0.18$, $Re = 15{,}390$	$Re = 21{,}304$	$T_{in} = 300$ K, $\varphi = 0.15$, $Re = 3500$		$T_{in} = 300$ K, $\varphi = 0.15$, $Re = 3500$	

2.2. Governing equations

For LES computations, we use the filtered continuity, momentum, species, and energy equations as stated below. In all the equations, the filtered variable is denoted by an overbar.

Continuity:

$$\frac{\partial \rho}{\partial t} + \frac{\partial}{\partial x_i}(\rho \overline{u}_i) = 0 \tag{1}$$

Momentum:

$$\frac{\partial}{\partial t}(\rho \overline{u}_i) + \frac{\partial}{\partial x_j}\left(\rho \overline{u}_i \overline{u}_j\right) = -\frac{\partial \overline{p}}{\partial x_i} + \frac{\partial \sigma_{ij}}{\partial x_j} - \frac{\partial \rho \tau_{ij}}{\partial x_j} \tag{2}$$

where σ_{ij} and τ_{ij} are the stress tensors due to the molecular viscosity and the subgrid-scale (SGS) stress, respectively. Their definitions are given as follows:

$$\sigma_{ij} \equiv \mu\left(\frac{\partial \overline{u}_i}{\partial x_j} + \frac{\partial \overline{u}_j}{\partial x_i} - \frac{2}{3}\delta_{ij}\frac{\partial \overline{u}_l}{\partial x_l}\right) \tag{3}$$

$$\tau_{ij} \equiv \overline{u_i u_j} - \overline{u}_i \overline{u}_j \tag{4}$$

For the sub-grid stress (SGS), the dynamic kinetic energy (DKE) model [38] is adopted, where the SGS kinetic energy is defined as $k_{sgs} = \frac{1}{2}\left(\overline{u_k^2} - \overline{u}_k^2\right)$. The k_{sgs} is used to compute the SGS eddy viscosity, ν_t defined as $\nu_t = C_k k_{sgs}^{1/2} \Delta_f$. Here, Δ_f is the filter-size calculated from $\Delta_f \equiv V^{1/3}$, where V is the volume of a computational cell. The SGS stress can then be rewritten in the following way:

$$\tau_{ij} - \frac{2}{3}k_{sgs}\delta_{ij} = -2C_k k_{sgs}^{1/2}\Delta_f \overline{S}_{ij} \tag{5}$$

where $\overline{S}_{ij}$ is the rate-of-strain tensor for the resolved scale defined by

$$\overline{S}_{ij} \equiv \frac{1}{2}\left(\frac{\partial \overline{u}_i}{\partial x_j} + \frac{\partial \overline{u}_j}{\partial x_i}\right) \tag{6}$$

For the SGS kinetic energy, k_{sgs} the following transport equation is solved.

$$\frac{\partial \overline{k}_{sgs}}{\partial t} + \frac{\partial \overline{u}_j \overline{k}_{sgs}}{\partial x_j} = -\tau_{ij}\frac{\partial \overline{u}_j}{\partial x_j} - C_\epsilon \frac{k_{sgs}^{3/2}}{\Delta_f} + \frac{\partial}{\partial x_j}\left(\frac{\nu_t}{\sigma_k}\frac{\partial k_{sgs}}{\partial x_j}\right) \tag{7}$$

The model constants in the above equations, C_k and C_ϵ, are determined dynamically, and σ_k is equal to 1.0.

Species transport:

$$\frac{\partial \rho \overline{Y}_{g,k}}{\partial t} + \frac{\partial}{\partial x_j}\left(\rho \overline{u}_j \overline{Y}_{g,k}\right) = -\frac{\partial J_{g,k}}{\partial x_j} + \overline{\dot{w}}_{g,k} - \dot{w}_{sgs,k} - \frac{\partial \rho \gamma_{jsgs,k}}{\partial x_j}, \left(k = 1, 2, \ldots, N_g\right) \tag{8}$$

where the species diffusion flux and the SGS mass flux are defined as follows:

$$J_{g,k} = -\rho D_{m,k}\frac{\partial Y_{g,k}}{\partial x_j} - \frac{D_{T,k}}{T}\frac{\partial T}{\partial x_j} \tag{9}$$

$$\gamma_{jsgs,k} = \overline{u_j Y_{g,k}} - \overline{u}_j \overline{Y_{g,k}} = \frac{\nu_t}{\sigma_{Y,k}}\frac{\partial \overline{Y_{g,k}}}{\partial x_j} \tag{10}$$

Energy:

$$\frac{\partial \rho \overline{h}}{\partial t} + \frac{\partial}{\partial x_j}\left(\rho \overline{h} \overline{u}_j\right) = \frac{\partial}{\partial x_j}\left(\frac{\mu}{Pr}\frac{\partial \overline{h}}{\partial x_j} - \sum_{k=1}^{n} \overline{h}_{g,k}\overline{J}_{g,k}\right) + S_h - \frac{\partial \rho q_{jsgs}}{\partial x_j} \tag{11}$$

where S_h is sources of energy due to chemical reaction. The diffusion fluxes, J_g are computed using Maxwell-Stefan and Fick's law diffusion coefficients [39] considering the thermal diffusion [40] for light species. The SGS heat flux is modelled as follows:

$$q_{jsgs} = \overline{u_j h} - \overline{u}_j \overline{h} = \frac{\nu_t}{\sigma_t}\frac{\partial \overline{T}}{\partial x_j} \tag{12}$$

In equations (9) and (11), the model constants σ_t and σ_Y are the SGS turbulent Prandtl number and Schmidt number, respectively which are obtained by the dynamic procedure proposed by Germano et al. [41].

Surface species coverage: $$\frac{d\theta_j}{dt} = \frac{\dot{s}_j}{\Gamma} = 0, (j = 1, 2 \ldots, N_s), \tag{13}$$

where θ is the surface species coverage, $\dot{s}$ is the surface species molar production rate and Γ is the surface site density.

To model heat transfer in solid, the heat conduction equation is stated as follows:

$$\frac{\partial \rho_s h_s}{\partial t} + \frac{\partial}{\partial x_j}\left(\lambda_s \frac{\partial T_s}{\partial x_j}\right) = 0 \tag{14}$$

2.3. Solutions algorithm and solver setting

A pressure-based solver was employed in Ansys Fluent 2023 R2 to solve the governing equations for turbulent flow variables using the Finite Volume Method (FVM). The incompressible filtered Navier-Stokes and species transport equations were discretised on a structured hexahedral grid. The discretised equations were solved in both space and time using the SIMPLE algorithm. In LES setting, the dynamic kinetic energy (DKE) subgrid-scale model is used to model the sub grid scale turbulence developed by Kim and Menon [38]. This model solves the transport equation of subgrid kinetic energy where model constants are determined dynamically. For the transient formulation, the bounded second-order implicit scheme was selected. For spatial discretisation, the least square cell-based method was used for gradients while the second-order method was used for pressure. The bounded central differencing scheme was used to compute convective fluxes. The stiff chemistry solver was chosen for thermochemistry, considering the integration method of ISAT (In situ adaptive tabulation). The Eddy-dissipation-concept (EDC) model of Gran et al. [42] was adopted to compute the gaseous reaction rates. Like EDC, a closure model is

essential for accurately describing turbulent catalytic rates. Arani et al. [29] showed that turbulence significantly impacts the transport of species like H_2 and O_2 at the catalytic surface, especially at high Reynolds numbers of 11,400 and 24,600, which are notably higher than those in our study. They also found that solids with high thermal inertia do not respond to temperature fluctuations induced by the reacting flow. In our study, the substantial wall thickness ($\delta = 0.5$ mm) results in high thermal inertia, which effectively dampens these temperature fluctuations at the catalytic surface. As a result, variations in temperature and concentration at the catalytic surfaces are minimal compared to their mean values. This diminishes the significant reaction nonlinearity typically associated with the Arrhenius exponential term. When nonlinearity does occur, it remains minimal under constant wall temperature conditions [23]. Consequently, the catalytic rates are modelled using a "laminar-like" closure, evaluated based on the surface temperature and the corresponding gas concentrations, as outlined in the referenced work [23]. Detailed chemical reaction mechanisms of catalytic (heterogeneous) and gas-phase (homogeneous) were employed. For homogeneous chemistry, the reaction mechanism of Warnatz et al. [43] was used, while the heterogeneous was obtained from Deutschmann et al. [44]. The validation of coupled (hetero-/homogeneous) reaction mechanisms was reported in previous studies [11,23]. CHEMKIN [45] and Surface-CHEMKIN [37] were used to evaluate the gaseous and surface reaction rates, respectively, while the transport properties were calculated using the CHEMKIN transport database [46]. However, we used the mass-weighted mixing law to calculate the viscosity and thermal conductivity of the mixture gas. To determine the mass diffusivity and thermal diffusion coefficient, the kinetic theory was applied.

Computations were performed on a High-Performance Computer (HPC) with Intel Xeon Gold 6138 (Skylake) processors at the ARCHIE-WeSt supercomputer centre using 40 cores. Computations were continued with a time step of 10^{-6}s until the flow reached a statistically steady state. The integration time to reach the steady states was 8 and 12 flow-through times for the planar and non-planar reactors, respectively. The LES statistics were averaged around 6 flow-through times for all the results reported here.

2.4. Mesh resolutions

Both the planar and non-planar configurations use a hexahedral grid to discretise the domains as shown in Fig. 2 (a) and Fig. 2 (b). In LES, large turbulent structures are directly resolved by the grid, while small-scale turbulence near the wall is captured using a subgrid-scale (SGS) model. Consequently, accurate wall treatment is essential in the LES methodology employed here to effectively capture the turbulent flow behaviour near solid boundaries. The grid resolution in the y-direction is mostly demanding and required to capture the most of flow fluctuations. In all cases, the near-wall grids are refined, with the first grid point placed at a non-dimensional wall distance, $y+$ (where $y+ = u_t \Delta y/\nu$) of less than 1.0. This allows the simulation to resolve the near-wall turbulence directly, without relying on wall functions. The spanwise z-direction has 70 grid points that are uniformly allocated, while the allocation of grid points in the streamwise x-direction is non-uniform. We used the grid resolutions (x-direction × y-direction) of 640 × 70, 180 × 60, and 250 × 70 in fluid domain for case 1 (C1), case 3 (C3-M1) and case 3 (C3-M2), respectively, in the planar reactor. The first grid point from the walls was placed at y+ = 0.54 for case 1 and y+ = 0.45 for case 3 (C3-M1), respectively, based on the maximum $y+$. For case 2 (C2) and case 4 (C4-M1), the total grid points in the x-direction were 740 and 630, respectively. The grid points between the reactor flat wall and full cylinder along the y-direction were 55 for case 2 and 35 for case 4, while the points between the two half cylinders along the y-direction were 60 for case 2 and 50 for case 4. The nearest grid point at the cylinder was placed at $y+ = 0.96$ for case 2 and $y+ = 0.92$ for case 4. Both C3 and C4 use solid domains to account for the conjugate heat transfer effect on catalytic combustion process. The number of grid cells for the simulated cases is summarised in Table 1. Fig. 3 compares the mean profiles of axial x-component velocity, temperature, mass fraction of H_2 species, and their fluctuations at $x/H = 7.5$ for two grids (C3-M1 and C3-M2) in the planar configuration. The comparison shows no significant difference in U_m, T_m and $Y_{m,H2}$ between the two grids, as presented in Fig. 3 (a), Fig. 3 (b), and Fig. 3 (c), respectively. However, the grid C3-M1 underpredicts fluctuations at the location of peak values. Similarly, for the non-planar configuration shown in Fig. 4, a grid test is conducted at $x/H = 7.23$ for two grid sizes (C4-M1 and C4-M2). In this case, the grid C4-M1 overpredicts U_m, T_m and $Y_{m,H2}$ at location of peak values as well as their fluctuations, as shown in Fig. 4 (a), Fig. 4 (b), and Fig. 4 (c), respectively.

2.5. Validation of the numerical solutions

The computational procedure of LES modelling in the planar and non-planar reactors shown in Fig. 1 is initially verified by reproducing the experimental catalytic reactor (case C1) of Appel et al. [23] and non-catalytic reactor (case C2) of Smith et al. [22]. Then, the effect of catalytic turbulent reacting flow for both the reactors (case C3 and case C4) is discussed and compared considering the same inflow condition and catalytic surface area. All the statistical parameters presented have been averaged over time and spanwise z-direction.

Fig. 5 shows the transverse mean profiles of velocity, species (H_2 and H_2O), temperature, and turbulent kinetic energy at different streamwise locations for the catalytic planar reactor. The results are compared with

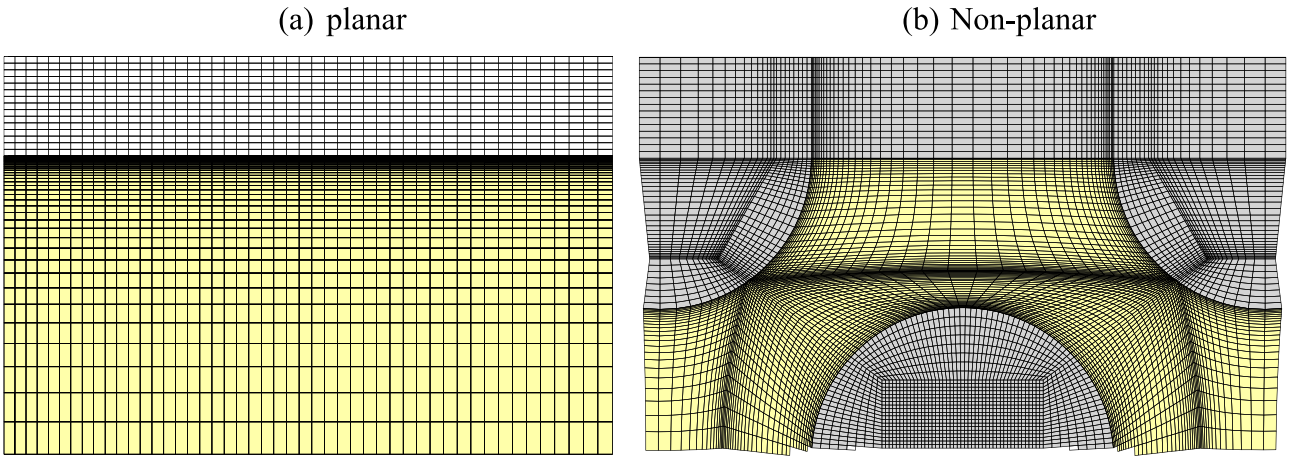

Fig. 2. Example of grid generation: (a) Generated grid for the planar reactor in case C3-M1, and (b) Generated grid for the non-planar reactor in case C4-M1.

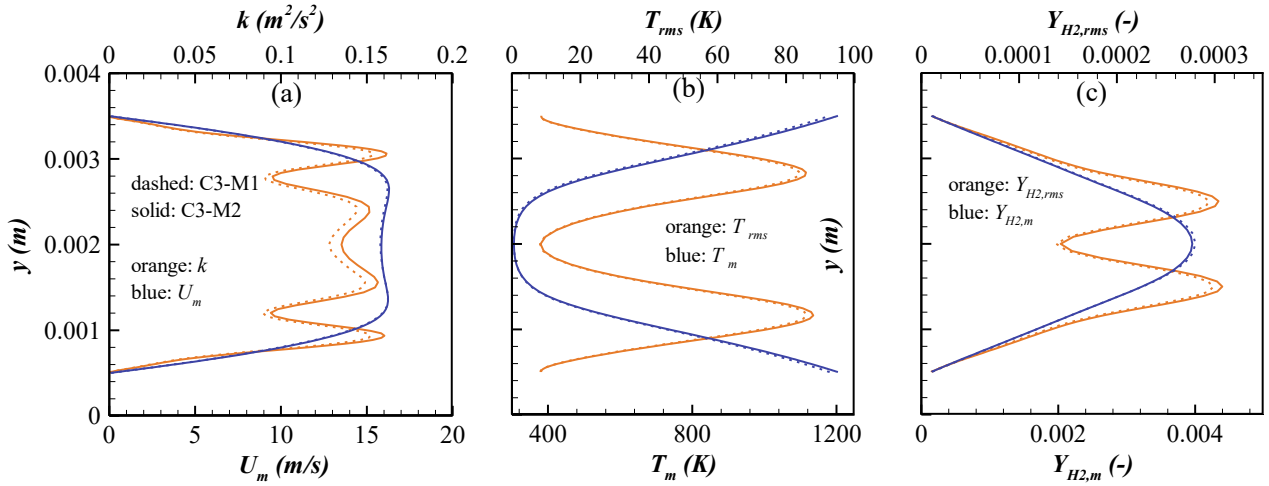

Fig. 3. Effect of grid resolution for the catalytic planar configuration (Case 3). Time averaged transverse profiles of (a) U_m and k, (b) T_m *and* T_{rms}, and (c) Y_{H2} and $Y_{H2,rms}$ at $x/H = 7.5$, $T_{in} = 300$ K, $\varphi = 0.15$ and $Re = 3500$.

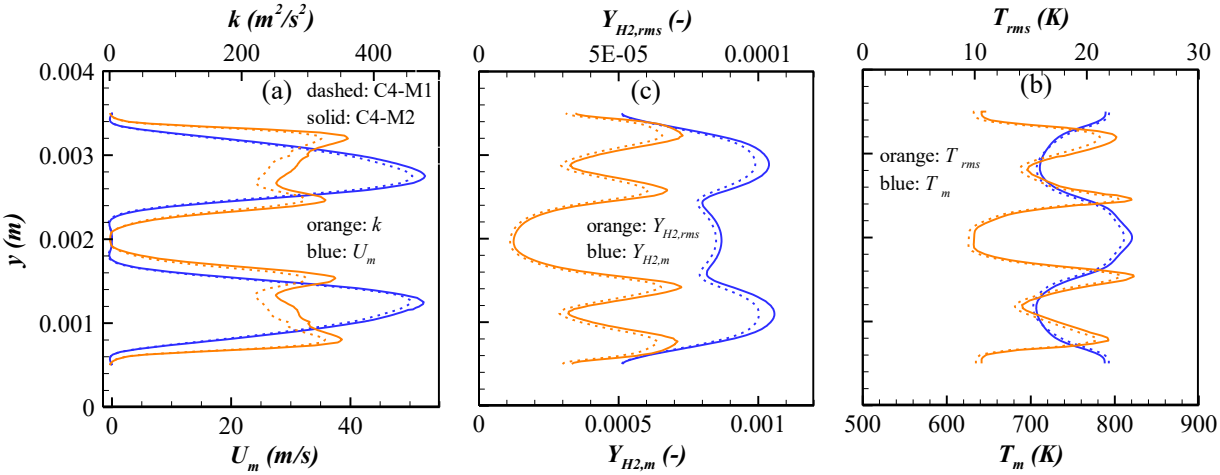

Fig. 4. Effect of grid resolution for the catalytic non-planar configuration (Case 4). Time averaged transverse profiles of (a) U_m and k, (b) T_m and T_{rms}, and (c) Y_{H2} and $Y_{H2,rms}$, at $x/H = 7.23$, $T_{in} = 300$ K, $\varphi = 0.15$ and $Re = 3500$.

the experimental data obtained from Appel et al. [23]. The present LES model captures well the continuous change of mean velocity (U_{avg}) and turbulent kinetic energy (k_{avg}) with increasing x in Fig. 5(a). The prediction of H_2 and H_2O over the reactor shown in Fig. 5(b) is in accord with the measurement data. However, there is a slight underprediction of H_2O at the far downstream near the wall regions. The reason is the limitation of the kinetic mechanism to produce the catalytic reaction process discussed in the previous studies [4]. Therefore, the underprediction of mean temperatures is observed at the similar locations shown in Fig. 5 (c). However, the measurement uncertainty reported for the species and temperature is ±10 % and ±50 K, respectively [23]. Overall, the LES predictions are satisfactory, and the same LES model is used to simulate the catalytic turbulent combustion process.

The catalytic reacting flow through a non-planar reactor, shown in Fig. 1(b), has not been studied before. Therefore, for LES validation in the non-planar reactor, the experimental study [22] of non-reacting flow (case C2) is simulated and compared. Fig. 6 shows the comparison of LES predictions for the mean velocity and turbulent quantities. The results are presented at the location of $x/H = 6.51$, midway between the full and half cylinders as the experimental results reported only that location. The predicted x- and y- components of mean velocity shown in Fig. 6 (a) and Fig. 6 (b), respectively, are in close agreement with the measurements. Again, the turbulent fluctuations in Fig. 6 (c)-(e) are generally captured well with the LES model. The only exception is the peak values of V_{rms} at the reactor core, where the level of deviation from the experimental results appears to be considerable due to the flow separation and reattachment in the wake region.

3. Results and discussion

In this Section, the validated LES model is used for the investigation of catalytic reacting flow in both the planar (case C3) and non-planar reactors (case C4) keeping the same inflow Reynolds number of 3500, inflow temperature of 300 K, and an equivalence ratio of 0.15. The catalytic surface area of 42.41 mm^2 is kept the same for both the configurations to allow for a comparison and better understanding of the catalytic process.

To visualise the flow field, Fig. 7 (a)-(c) illustrates the contours of the instantaneous axial velocity (U), mean axial velocity (U_m), and its fluctuations (U_{rms}) for the planar catalytic reactor. In Fig. 7(b), it is shown that the mean velocity increases along the length of the reactor. The U_{rms} level in Fig. 7(c) is at its minimum at the catalytic wall and increases as the distance from the wall increases. Notably, the U_{rms} level is low at the reactor core and in a distinct region between the reactor core and the wall. However, to better understand the impact of reacting flow on the flow field, a non-reacting case under isothermal conditions, with the

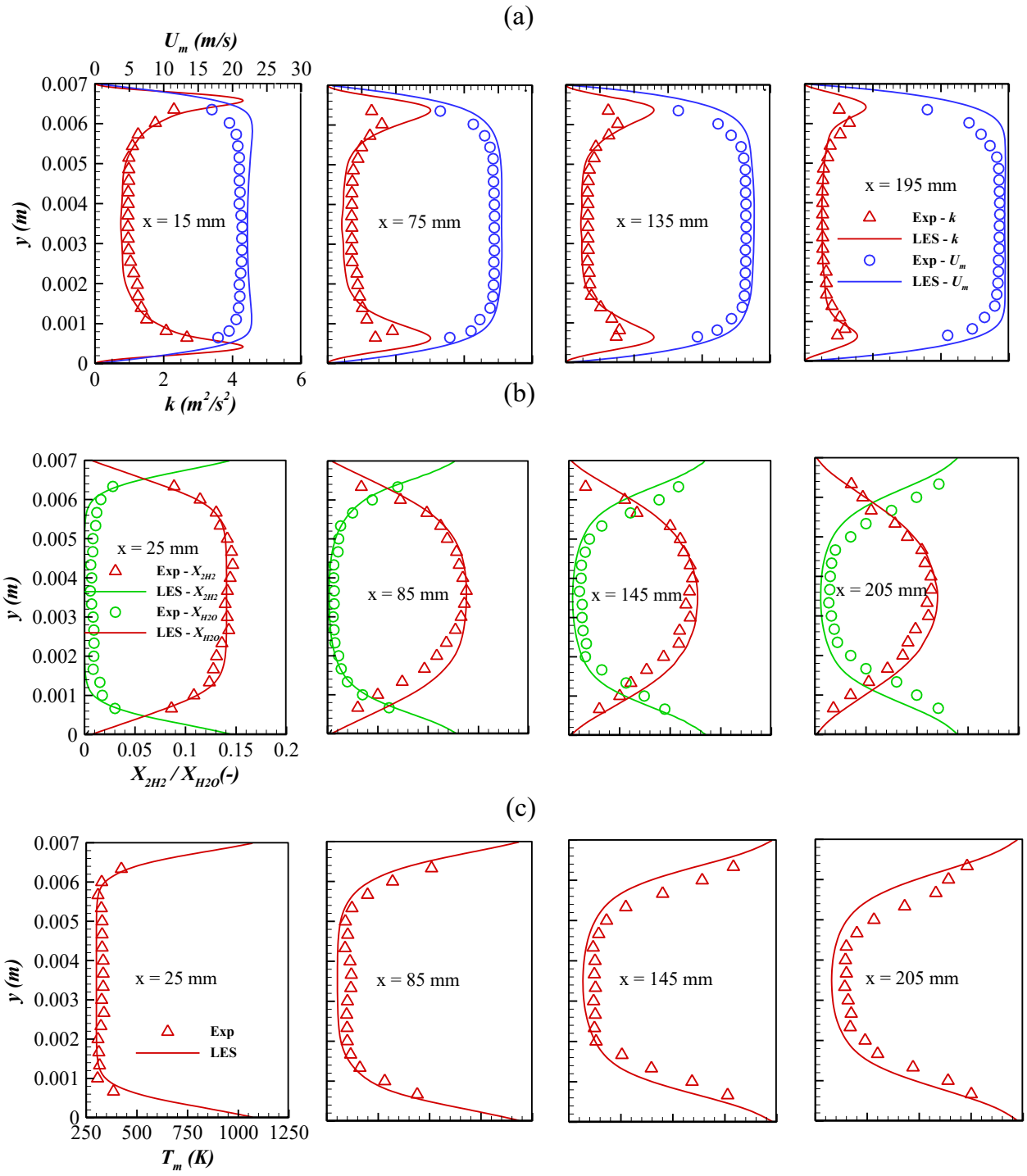

Fig. 5. Case C1 (reacting): LES comparison at various streamwise locations for the time-averaged mean profiles of (a) U_m and k, (b) X_{H2} and X_{H2O}, and (c) T_m, at T_{in} = 300 K, φ = 0.18, Re = 15,390.

same inflow Reynolds number, is also simulated. Fig. 7(d)-(i) and Fig. 8 (a)-(f) presents the transverse profiles of the mean velocity and its fluctuations at five different axial locations for reacting and non-reacting case, respectively. As shown in Fig. 7(d) for U_m in reacting flow, there is a characteristic overshooting of fast fluids near the wall. Consequently, U_m is at a high level near the wall and decreases to a low level at the reactor centre. As the downstream distance (x) increases, the U_m rises significantly compared to the non-reacting case, as shown in Fig. 8(a), due to the heat release from the catalytic wall. Again, the peak overshoot moves towards the reactor centre with increasing x, indicating the development of a growing boundary layer. This type of velocity profile shows the effect of flow laminarisation reported in the literature [47]. To illustrate the laminarisation effect, the turbulent kinetic energy (k) for the reacting and non-reacting cases is compared at the same locations in Fig. 7(e) and Fig. 8(b), respectively. As shown in Fig. 8(b) for the non-reacting case, k exhibits peaks near the wall and maintains the similar levels across different axial locations, though k at the reactor core decreases as x increases. In contrast, for the reacting flow in Fig. 7(e), k is low near the wall but high at the centre at $x/H = 3.0$. Initially, k near the wall decreases and then increases with x, indicating an intensification of

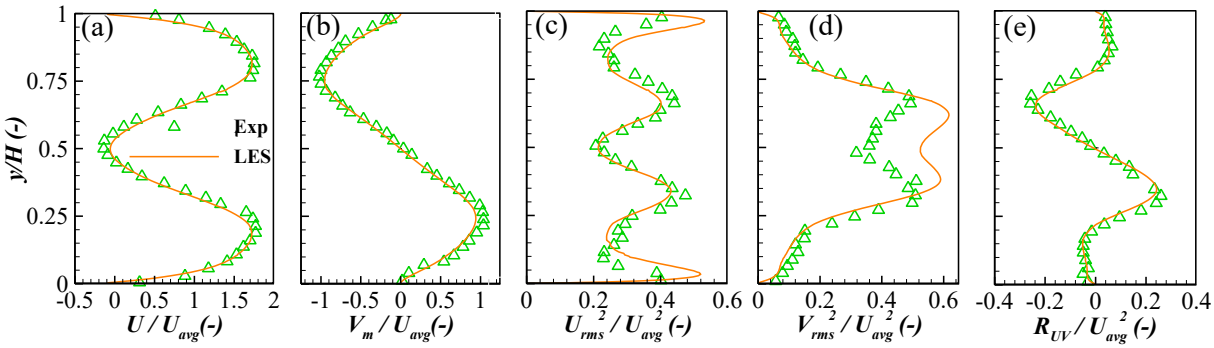

Fig. 6. Case C2 (non-reacting): LES comparison for the time-averaged mean velocity (U_m and V_m) and Reynold stresses (R_{UV}) at $x/H = 6.51$, $Re = 21{,}304$.

turbulence. However, the k values near the wall are significantly lower compared to those in the non-reacting case in Fig. 8(b), although the values at the reactor centre remain relatively consistent. This observation aligns with the previous findings in catalytically turbulent reacting flows in channels [25,29]. The characteristics of laminarising the flow and intensifying the turbulence near the wall are described as a two-stage process [28,48]. For instance, near the catalytic walls, heating induces local volumetric expansion, which enhances the ejection of low-speed hot fluid away from the walls. Initially, this effect is minor compared to the viscosity's impact on turbulence, resulting in laminarisation of the flow near the wall. However, as the distance x increases, this effect begins to counterbalance the viscosity's damping influence on turbulence, leading to an increase in k. Moving towards the reactor core, the ejection motion of hot fluid strengthens compared to the viscosity effect, resulting in a balance that slightly increases streamwise turbulence. Again, k exhibits two peaks near the reactor core in locations far downstream. This occurs due to the mixing of hot and cold fluids within the developing boundary layer. As described in [48], this mixing is driven by the ejection motion of hot fluids toward the reactor core and the sweep motion of cold fluids toward the wall, with the former dominating, leading to the observed downstream peaks. The transverse profiles of fluctuating components at these locations are presented in Fig. 7(f)-(i). As previously discussed, due to the same reasons, the U_{rms} shows a similar trend to k in Fig. 7(f), with near-wall values being lower compared to those in the non-reacting case shown in Fig. 8(c). Both V_{rms} and W_{rms} in Fig. 7(g)-(h) have small values near the wall and large values at the reactor core, and they decrease with x [28,29]. In comparison, the non-reacting case in Fig. 8(d)-(e) shows no significant variation in these quantities. However, the overall impact of velocity fluctuations throughout the reactor can be observed in the Reynolds stress (R_{UV}) profiles shown in Fig. 7(i). The R_{UV} exhibits peaks with both positive and negative values that correlate with the sign and magnitude of the velocity gradient [47]. The R_{UV} has the opposite sign to the velocity gradient and vanishes where the velocity gradient is zero. As reported in [47,49,50], the R_{UV} peak occurs at locations of peak U_{rms} and the R_{UV} value is zero at locations where U_{rms} is at a trough. The R_{UV} values near the wall in the reacting case are similar to those in the non-reacting case, as shown in Fig. 8(f). However, the R_{UV} peaks in reacting flow are higher near the reactor core, confirming the process of turbulent intensification caused by the ejection of hot fluids toward the reactor core.

Fig. 9 illustrates the temperature and species distributions for the planar reactor. As shown in Fig. 9(a), the hot catalytic surfaces transfer heat to both the fluid and the solid. The conducted heat in the solid is directed towards the inert region near the inlet and outlet, preheating the incoming fresh mixture and the exiting combustion product, respectively. The fluid temperatures are high near the walls and low in the reactor core. The transverse profiles of the mean temperature (T_m) and its fluctuations (T_{rms}) are shown in Fig. 9(e)-(f) at different axial locations and, are symmetric about the reactor midplane on the y-axis. The results indicate that the cylinder core temperature remains below 400 K. However, unlike velocity fluctuations, T_{rms} in Fig. 9(f) increases with two peaks shifting towards the reactor core as x increases. This noteworthy aspect is explored based on the DNS predictions of Bae et al. [50], which consider classical heat transfer in a channel flow case. Their findings indicate that the wall heating reduces velocity fluctuations but has no significant effect on the T_{rms} predictions. As mentioned in their report, the underlying reason is that the enthalpy fluctuation remains at a considerable level downstream with the flow (for further details see [50]). Therefore, there seems to be no evidence supporting the notion that the effects of heating on the velocity and temperature fluctuations in turbulent flows are similar.

The mass fraction distribution of H_2 for the catalytic planar reactor is presented in Fig. 9(b). The H_2 concentration is high near the inert walls before entering the catalytic section. This is because of the high-affinity H_2 towards the hot walls reported by Mondal et al. [23]. As expected, due to the catalytic process, H_2 is consumed on the catalytic surfaces, leaving the reactor core unburned. Fig. 9(c) shows the distribution of instantaneous H_2O production in the catalytic planar reactor. The concentration of H_2O is high in the area where catalytic combustion occurs. Under the fuel-lean conditions, as discussed in a previous article [11], the mode of combustion here is mainly catalytic. However, the instantaneous contour of OH is presented in Fig. 9(d) to further investigate the role of homogeneous (gas phase) combustion. The Y_{OH} scale is kept low, up to 2×10^{-5}, to capture the onset of homogeneous combustion. Since the catalyst produces less OH, the relatively low Y_{OH} levels on the catalytic surfaces is an indication of weak combustion of the gas mixtures. Additionally, this low OH levels may result from the catalyst consuming OH produced by homogeneous combustion, thus inhibiting the combustion process. [11]. To provide further clarity, the streamwise profiles of the locally averaged (upper and lower surfaces) catalytic (C) and the integrated gas-phase (G) H_2 conversion rates are illustrated in Fig. 10(a). The results demonstrate that gas-phase conversion rates are significantly lower than catalytic rates, and both catalytic and homogeneous combustion can occur simultaneously at the same location. Following the catalytic sections, the Y_{OH} levels result from the growth of the OH boundary layer near the hot inert wall with the flow.

Fig. 9(g)-(h) presents the H_2 transverse profiles of time-averaged mean and fluctuations at different axial locations. The $Y_{H2,m}$ level in Fig. 9(g) is low on the catalytic surface and increases with distance from the catalytic surface. The $Y_{H2,m}$ values decrease as x increases. The maximum $Y_{H2,m}$ value near the end of the catalytic section is above 0.0038. Beyond that point, the $Y_{H2,m}$ values decrease in the reactor core and increase near the inert wall because of the characteristics of H_2 towards the hot walls. Like the temperature fluctuations (T_{rms}), the $Y_{H2,rms}$ in Fig. 9(h) has two peaks which increase with x and shift towards the reactor core. Similar observations of $Y_{H2,rms}$ were reported in an experimental work on catalytic combustion of hydrogen in a channel [51]. This indicates that the wall heating does not suppress the H_2 fluctuations. After the catalytic section at $x/H = 9$, the $Y_{H2,rms}$ values

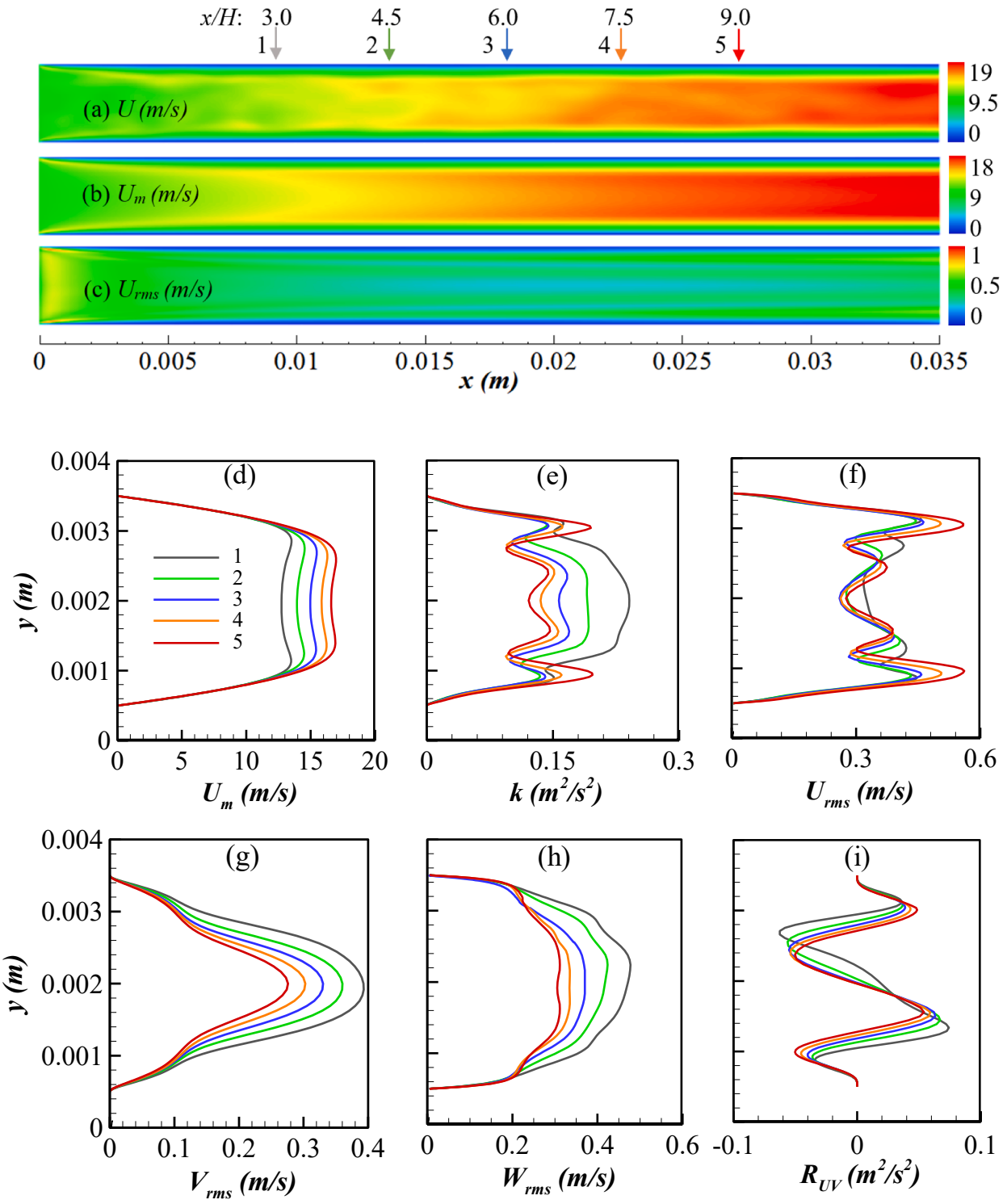

Fig. 7. Case 3 (reacting): Contours of (a) instantaneous x-velocity, U, (b) time-averaged mean x-velocity, U_m and (c) its fluctuations, U_{rms} onto the xy-plane at $z/H = 0.75$. Transverse profiles of time-averaged (d) U_m (e) k (f) U_{rms} (h) V_{rms} (h) W_{rms} and (i) R_{UV} (or $U_{rms}V_{rms}$) at five streamwise locations.

increase significantly near the inert walls due to H_2 distribution while the $Y_{H2,rms}$ peak values remain similar in the reactor core.

To assess the heat and H_2 mass exchange between the flow and catalytic surfaces, the Nusselt number (Nu) and Sherwood number (Sh) of H_2 for the planar reactor are calculated on the reactor inner surface and shown in Fig. 10(b). The presented Nu and Sh values are the averages of those from the upper and lower surfaces of the planar reactor. Their definitions are given as follows:

Nusselt Number:

$$Nu = \frac{h_c(2H)}{\lambda_g} \quad \text{where} \quad h_c = \frac{\lambda_g \frac{\partial T}{\partial y}\Big|_{wall}}{T_w - T_{ref}} \tag{15}$$

where h_c is the heat transfer coefficient, λ_g is the fluid conductivity and $\partial T/\partial y$ is the gradient of temperature at the solid surface. The T_w and T_{ref}

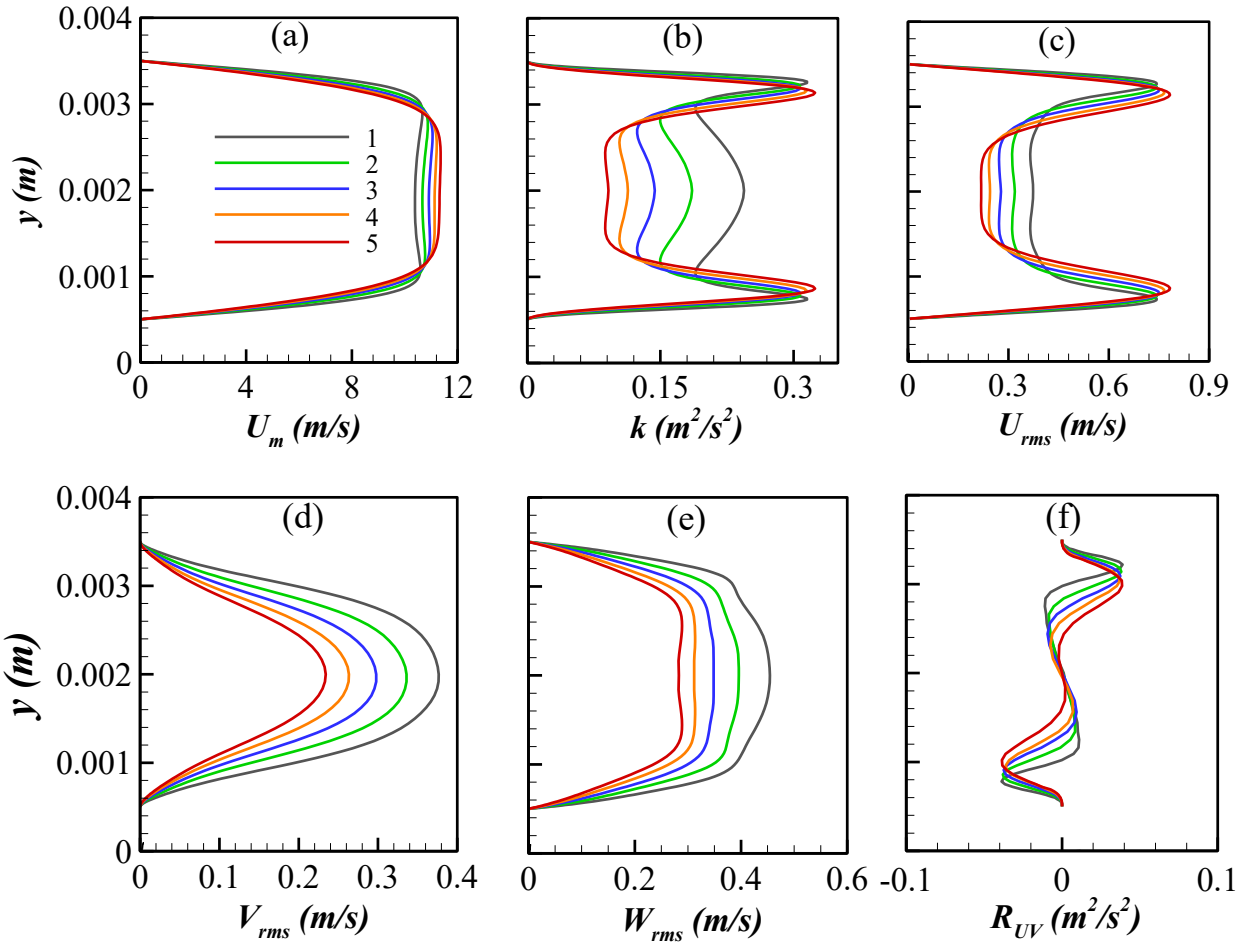

Fig. 8. Case 3 (non-reacting): Transverse profiles of time-averaged (a) U_m (b) k (c) U_{rms} (d) V_{rms} (e) W_{rms} and (f) R_{UV} (or $U_{rms}V_{rms}$) at five streamwise locations.

are the wall surface and the reference temperatures, respectively. For convenience, T_{ref} is the average of T_{in} and T_{adb} where T_{adb} is the adiabatic temperature of H_2/air mixture. In Fig. 10(b), *Nu* is high at the entrance of the reactor and gradually decreases along the length of the reactor. This is because the thermal boundary layer is thin at the entrance, causing a high temperature gradient and a high value of *Nu*. As the fluid flows along the reactor length, the thermal boundary layer thickens and the temperature gradient decreases, resulting in a decrease in *Nu*.

Sherwood Number:

$$Sh = \frac{k_c(2H)}{D_m}, \quad \text{where} \quad k_c = \frac{D_m \frac{\partial C_{H2}}{\partial y}\Big|_{wall}}{C_{H2,w} - C_{H2,ref}} \tag{16}$$

where k_c and D_m are the H_2 mass transfer coefficient and mass diffusivity, respectively. $\partial C_{H2}/\partial y$ is the gradient of mean H_2 mass concentration at surface. $C_{H2,w}$ and $C_{H2,ref}$ are the surface and the reference concentration of H_2, respectively. $C_{H2,ref}$ is considered as an average of concentrations at T_{in}, and at T_{adb} where H_2 is considered to be completely consumed.

As shown in Fig. 10(b), the *Sh* is high at the beginning of the channel due to a high H_2 concentration gradient caused by thermal diffusion. This value gradually decreases as the concentration boundary layer develops in the inert region. The boundary layer disruption, caused by catalytic combustion, results in a high *Sh* at the beginning of the catalytic section, which then significantly drops up to $x = 0.01$. Beyond this point, the variation in *Sh* remains insignificant with increasing x up to the end of the catalytic section. Initially, the H_2 concentration rate at the catalytic surface is high, resulting in a steep H_2 concentration gradient and a high *Sh* value. As x increases, the concentration level becomes insufficient for effective catalytic combustion, leading to a decreased concentration gradient and, consequently, a lower *Sh*. After the catalytic section, the H_2 concentration near the wall increases due to the standard Fickian diffusion, causing a further decrease in the H_2 concentration gradient, and thus, resulting in an insignificant effect of *Sh* in the inert region. However, the *Nu* and *Sh* in Fig. 10 (b), exhibit different behaviours, indicating that the typical mass and heat transfer analogy does not apply in this case due to catalytic combustion affecting the wall temperatures and fluid properties. Additionally, the wall shear stress (τ_w) along the reactor is shown in Fig. 10(b). τ_w is initially high at the entrance due to the developing boundary layer, and then it gradually decreases. This decrease is attributed to increased viscosity caused by heat transfer from the wall. Overall, the behaviours of Sherwood and Nusselt number and the shear stress appear to be quite different. Hence, considering the catalytic process, the general analogy among momentum, heat, and mass transfer does not seem to be totally applicable.

Fig. 11(a)-(c) illustrates the flow field of the non-planar catalytic reactor. The contours of the instantaneous x-velocity (U) and mean x-velocity (U_m) in Fig. 11(a)-(b) reveal the presence of a recirculation zone across the domain, attributed to the flow restriction caused by the cylindrical rods. This recirculation occurs predominantly at the back of the cylinders. The flow velocity rises above and below the cylinders, resulting in increased streamwise velocity fluctuations (U_{rms}) shown in Fig. 11(c). Both the U_m and U_{rms} velocity fields are relatively symmetric about the reactor midplane on the y-axis. The strongest magnitudes of U_{rms} are located above and below full cylinder 3 and its neighbouring half-cylinders. This is due to the adjacent heated walls resulting from the

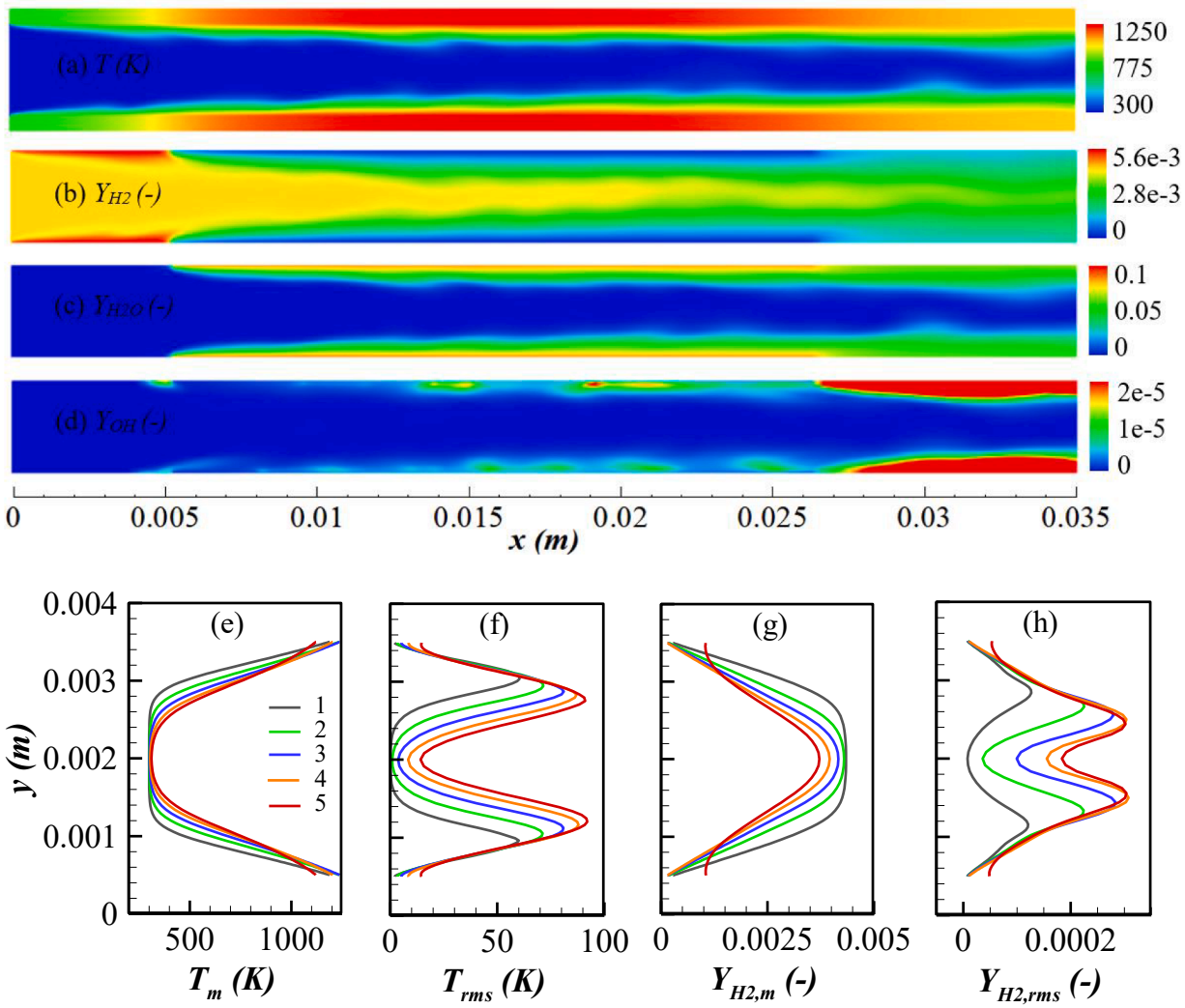

Fig. 9. Case 3 (reacting): Instantaneous contour of (a) T (b) Y_{H2} (c) Y_{H2O} (d) Y_{OH} onto the xy-plane at $z/H = 0.75$; Transverse profile of (e) T_m (f) T_{rms} (g) $Y_{H2,m}$ (h) $Y_{H2,rms}$, the number from 1 to 5 indicates axial locations shown in Fig. 7(a).

catalytic combustion causing fluid expansion. To better understand this effect, the transverse distribution of mean axial velocity and turbulent fluctuations at different axial locations are shown in Fig. 11(d)-(h). The locations are considered downstream of full cylinders, indicated by the vertical lines and numbered from 1 to 6 in Fig. 11(a). As shown in Fig. 11 (d), the peak of U_m occurs between the half and full cylinders, while the troughs are located at the back of the full cylinders, which are wake zones due to flow separation. The U_m peak values at location 2 increase significantly and become, nearly 1.5 times compared to location 1. At locations 2 and 3, the peak values are similar but increase again at locations 4 and 5. Subsequently, the peak values at locations 5 and 6 remain similar and become, nearly 1.85 times compared to location 1. As mentioned earlier, the heat transfer form hot catalytic surfaces to fluid here is strong causing fluid expansion and high streamwise velocity. This also significantly affects the velocity fluctuations (U_{rms},V_{rms} and W_{rms}) shown in Fig. 11(f)-(i). The fluctuations successively increase at locations 2 and 3 compared to 1. After that, the variations at locations 4, 5, and 6 become smaller. However, to analyse the laminarisation effect, the turbulent kinetic energy (k) is presented in Fig. 11(e). Unlike that in the planar reactor, the value of k increases with streamwise locations, indicating a strengthening of turbulent flow. Furthermore, the resolved Reynolds stress (R_{UV}) variations at the same locations are shown in Fig. 11(i). Similar to the velocity fluctuations and k, the R_{UV} peaks also increase with streamwise locations, confirming the intensified turbulent effects in the nonplanar reactor.

Fig. 12(a)-(d) illustrates the contour of instantaneous temperature and species mass fraction for the non-planar reactor. As shown in Fig. 12 (a), the fluid temperatures are high near the walls and cold far from the walls up to the 4th full cylinder. As effective heat transfer occurs from the wall to the fluid, the temperature variations diminish significantly, leading to nearly uniform temperatures far downstream. The transverse profile of the mean temperature (T_m) and the temperature fluctuations (T_{rms}) for the non-planar reactor are presented in Fig. 10(e) and Fig. 12 (f), respectively. As discussed earlier, T_m values are high near the walls due to heating provided by the catalytic walls and minimum far from walls. The T_m increases significantly up to location 5 and beyond that, the variation between locations 5 and 6 becomes smaller, indicating a weakening of the catalytic combustion process though temepature by itself is insufficient for judging the strength of catalytic reactions. In Fig. 12(f), the T_{rms} has peaks in the regions between half and full cylinders. The T_{rms} peak values exceed 80 K and are highest at locations 2 and 3. An interesting observation is that T_{rms}, compared to the planar reactor, exhibit low values at far downstream locations, even though the velocity fluctuations are high. This observation reaffirms the minimal impact of wall heating on temperature fluctuations, as discussed earlier in Fig. 9(f) for planar reactor. It also emphasises that the enthalpy

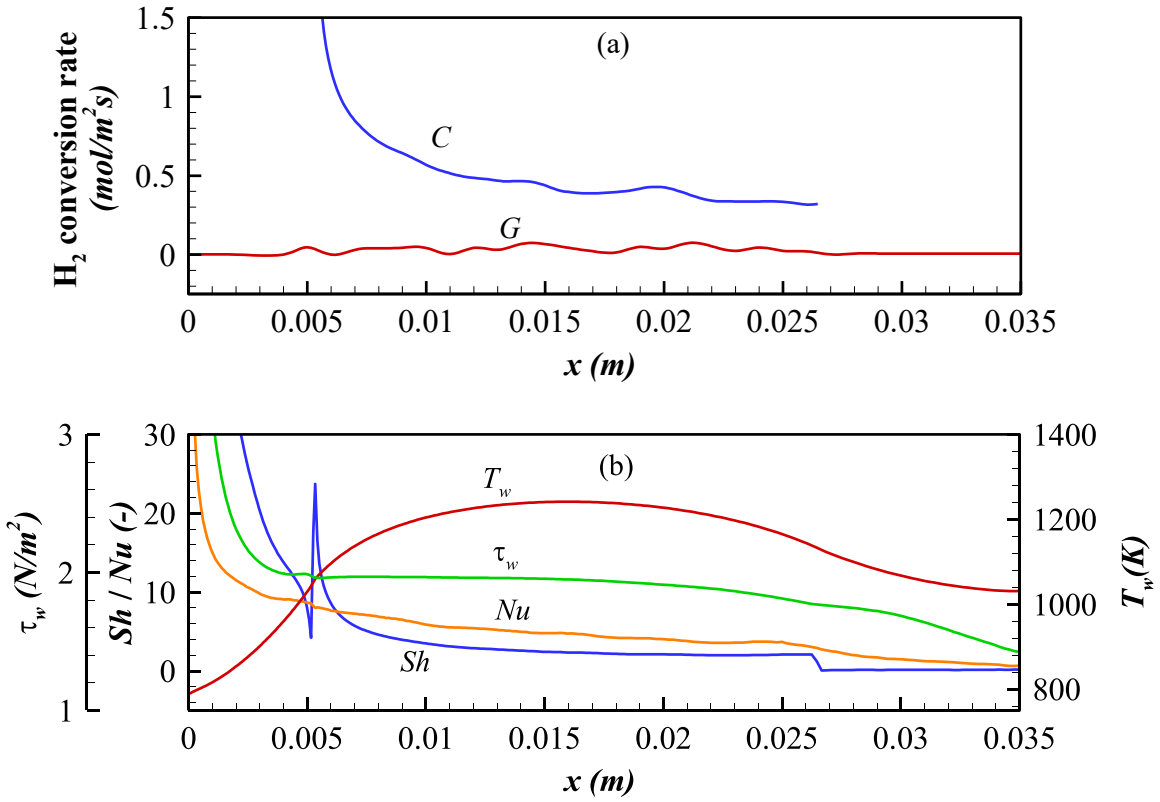

Fig. 10. Case 3 (reacting): (a) The predicted locally averaged (upper and lower surfaces) catalytic conversions (C) and the integrated (over the reactor flow height) gaseous conversions (G) along the streamwise direction. (b) Local distribution of Nu, Sh, τ_w and T_w on reactor inner surface.

fluctuation as reported in article Bae et al. [50] plays a significant role in temperature fluctuations.

The mass fraction of H_2 shown in Fig. 12(b) decreases along the streamwise direction in a non-planar reactor, due to catalytic combustion on the Pt-coated cylindrical surfaces. Compared to planar reactor, H_2 consumption is more effective, owing to the increased mass transfer of H_2 with the flow towards the catalytic surfaces. To gain a better understanding, the mean and fluctuation of the mass fraction of H_2 transverse distribution at six axial locations are presented in Fig. 12(g) and Fig. 12(h), respectively. These axial locations are shown in Fig. 11. The $Y_{H2,m}$ values for non-planar reactor, shown in Fig. 12(g), significantly decrease up to location 5 and beyond that, the variations become smaller. Similar behaviour is also observed in the temperature profile discussed in Fig. 12(e). This is due to insufficient H_2 concentration available for the catalytic process. The maximum $Y_{H2,m}$ value at the location 6 drops below 0.0012. The $Y_{H2,rms}$ in Fig. 12(h) has a nearly identical profile to T_{rms} with peaks in the regions between half and full cylinders. The $Y_{H2,rms}$ peak values are highest at locations 2 and 3 shown in Fig. 12(h). After these locations, the $Y_{H2,rms}$ peak values gradually decrease with increasing x. These observations of the non-planar reactor, along with the results for the planar reactor in Fig. 9(f) and Fig. 9(h), indicate that H_2 mass fraction fluctuations are strongly linked to temperature fluctuations.

In contrast to the planar reactor, the combustion process in the non-planar reactor is entirely catalytic, as indicated by the absence of significant OH throughout the domain, as seen in Fig. 12(c). For further confirmation, the locally averaged catalytic (C) and the integrated gas-phase (G) H_2 conversion rates are presented in Fig. 12(i). The flat profile with zero conversion rates indicates the absence of homogeneous combustion under the current operating conditions. Fig. 12(d) shows the instantaneously produced H_2O distribution resulting from catalytic reactions within the reactor. The H_2O concentration increases along the length of the reactor, with the variation becoming smaller after $x \approx 0.018$. This is because the low concentration of H_2 limits further catalytic combustion.

However, the distribution of Nu and Sh of H_2 species over the catalytic surfaces along the length of the non-planar reactor is shown in Fig. 13(a) and Fig. 13(b), respectively. Due to symmetry, both Nu and Sh are averaged from the values of the upper and lower cylindrical surfaces. As expected, close to the stagnation points of the cylinders where the boundary layers are thin, Nu and Sh values are high. The opposite applies to the wake region at the back of cylinders. This is why, the quarter portion at the back of the cylinder is uncoated. However, both the Nu and Sh peaks occur in most of the cylindrical surfaces at an angle of about 22.5. The peak Nu and Sh values up to $x = 0.014$ on cylinders are high compared to downstream cylinders, indicating more effective catalytic processes in these regions. As a result, significant variations in turbulent quantities discussed earlier are observed in those regions. However, the wall shear stress distribution (τ_w) over the cylindrical surfaces is shown in Fig. 13(c) to relate the overall impact of flow on heat and mass transfer. As seen in the plot, the τ_w significantly increases from the stagnation point because of the high velocity gradient and becomes a peak at a similar location of Nu peak. After that, the τ_w decreases as velocity gradient decreases.

Fig. 14 shows the hydrogen conversion along the reactor length. Conversion values are obtained using the following formula:

$$H_2 \text{ conversion } (\%) = \frac{Y_{H2,avg,in} - Y_{H2,avg,x}}{Y_{H2,avg,in}} \times 100 \tag{17}$$

where $Y_{H2,avg,in}$ and $Y_{H2,avg,x}$ are the average H_2 mass fraction at the inlet and axial positions, respectively. The $Y_{H2,avg}$ values are estimated at streamwise locations taking into account the spatially averaged transverse and spanwise directions. With the same amount of catalytic surface area, the non-planar reactor achieves a significantly higher H_2 conversion rate. Although the residence time may slightly differ between the two reactors, this conversion rate remains a useful metric for

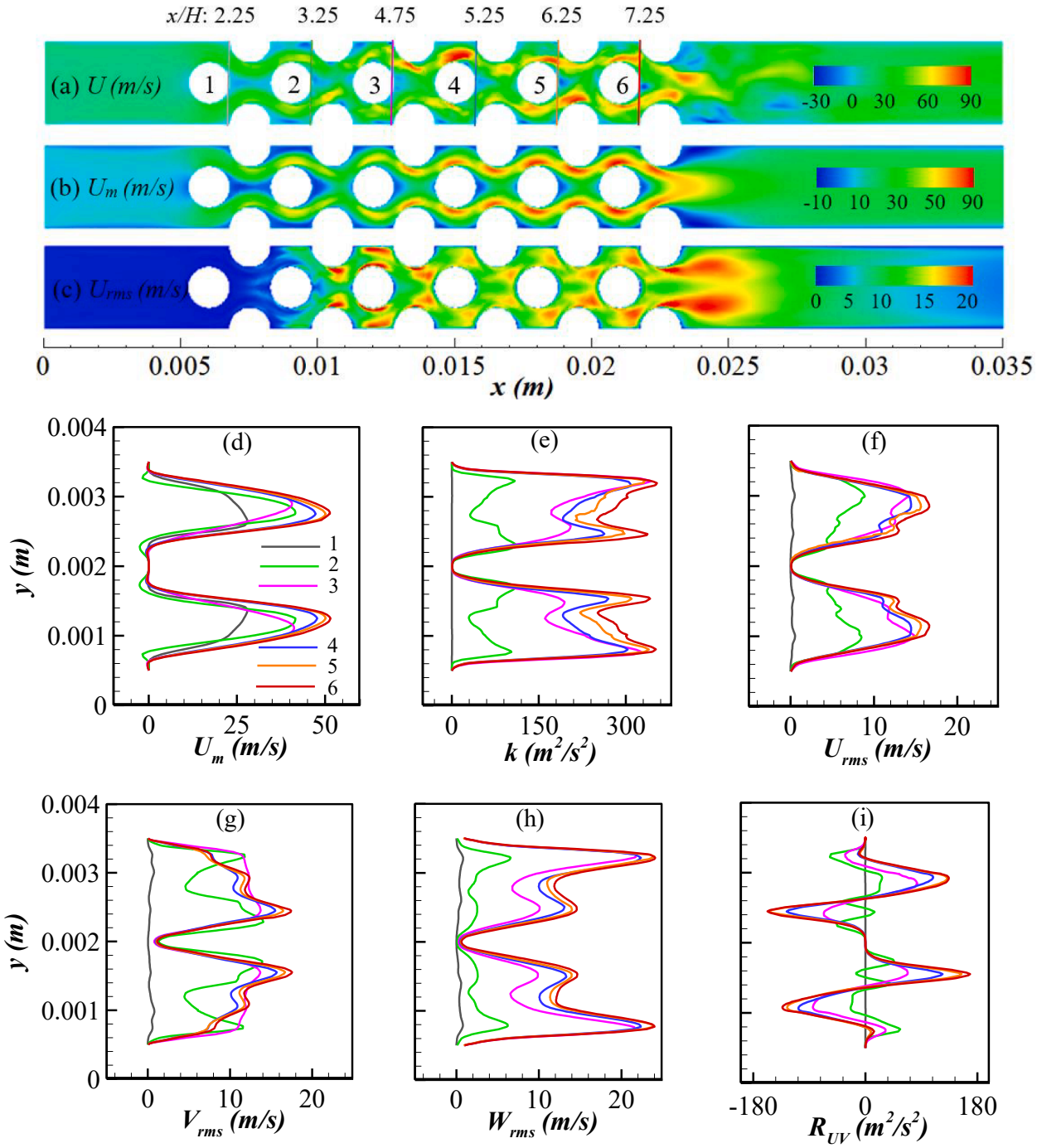

Fig. 11. Case 4 (reacting): Contours of (a) instantaneous x-velocity, U (b) time-averaged mean x-velocity, U_m and (c) its fluctuations, U_{rms} onto the xy-plane at $z/H = 0.75$ Transverse profiles of time-averaged (d) U_m (e) k (f) U_{rms} (g) V_{rms} (h) W_{rms} and (i) R_{UV} (or $U_{rms}V_{rms}$) at six streamwise locations.

comparing their effectiveness. As previously discussed, the cylindrical rods placed across the flow in the non-planar reactor significantly enhance the mass transfer of H_2 towards the catalytic surface, thereby improving the catalytic combustion process. Notably, the first ~60 % H_2 conversion is achieved using only 50 % of the catalyst, whereas the remaining catalyst contributes to an additional ~20 % H_2 conversion. In contrast, the planar reactor achieves ~37 % and ~11 % H_2 conversion for the first and second 50 % of the catalyst, respectively. Interestingly, the initial 37.5 % of the catalyst in the non-planar reactor can achieve the same output as the entire planar reactor.

The non-planar reactor, while advantageous, experiences a significant pressure drop of 97.2 %, compared to 48.7 % in the planar reactor. This drop, defined as the percentage decrease from the inlet pressure, results from the flow separation and constriction caused by the cylinders placed inside the reactor. In the catalytic reactor design, balancing the H_2 conversion efficiency with the pressure drop is crucial, impacting throughput, energy efficiency, and costs. Future work should focus on the further optimisation of reactor geometry to improve flow distribution as well as the refining catalyst coating strategies to achieve this balance.

3.1. Discussion

Catalytic hydrogen combustion in a planar type reactor has been

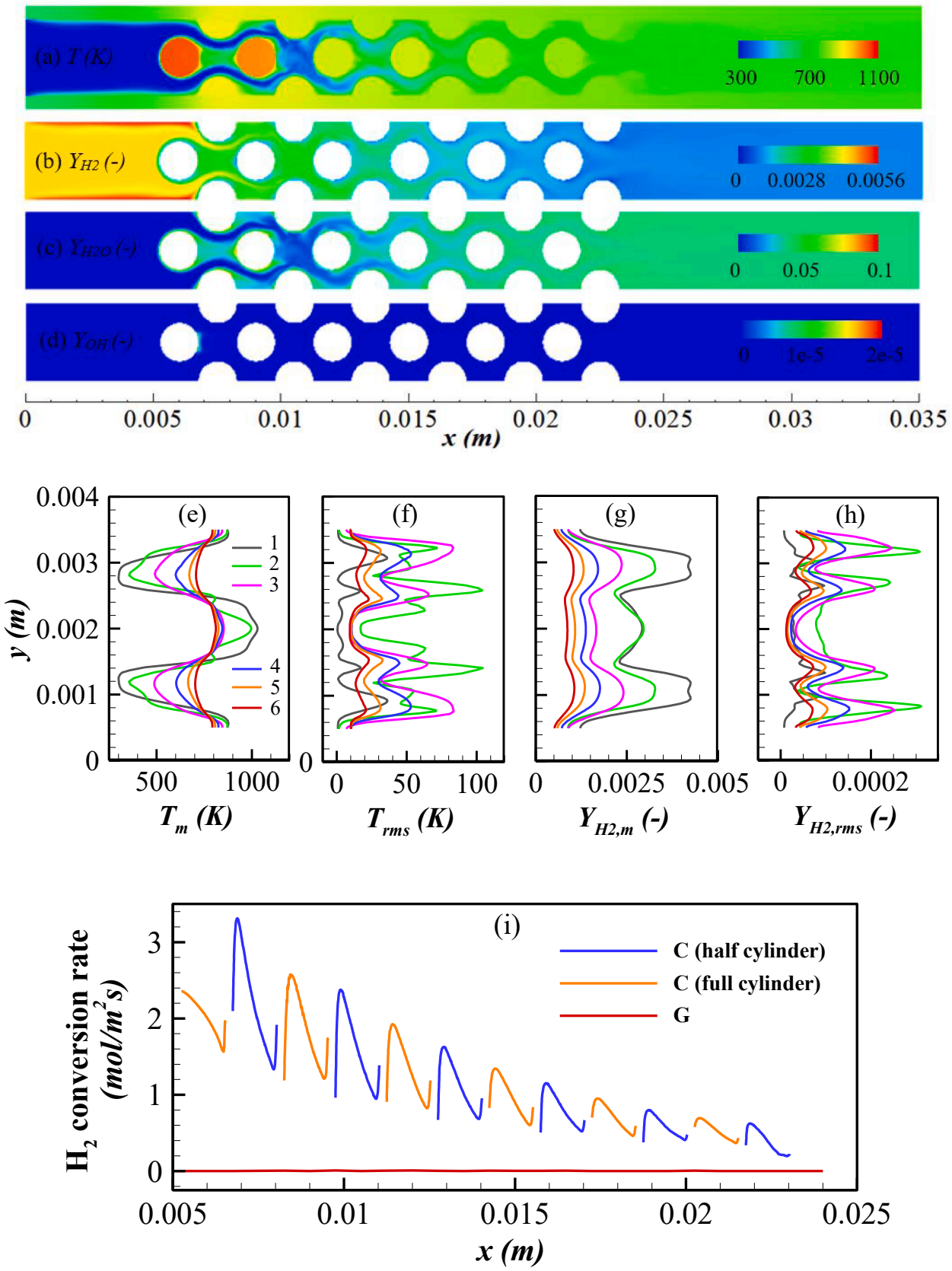

Fig. 12. Case 4 (reacting): Instantaneous contour of (a) T (b) Y_{H2} (c) Y_{H2O} (d) Y_{OH} onto the xy-plane at $z/H = 0.75$; Transverse profile of (e) T_m (f) T_{rms} (g) $Y_{H2,m}$ (h) $Y_{H2,rms}$, the number from 1 to 6 indicates axial locations shown in Fig. 8(a) (i) The predicted locally averaged (upper and lower cylindrical surfaces) catalytic conversions (C) and the integrated (over the reactor flow height) gaseous conversions (G) along the streamwise direction.

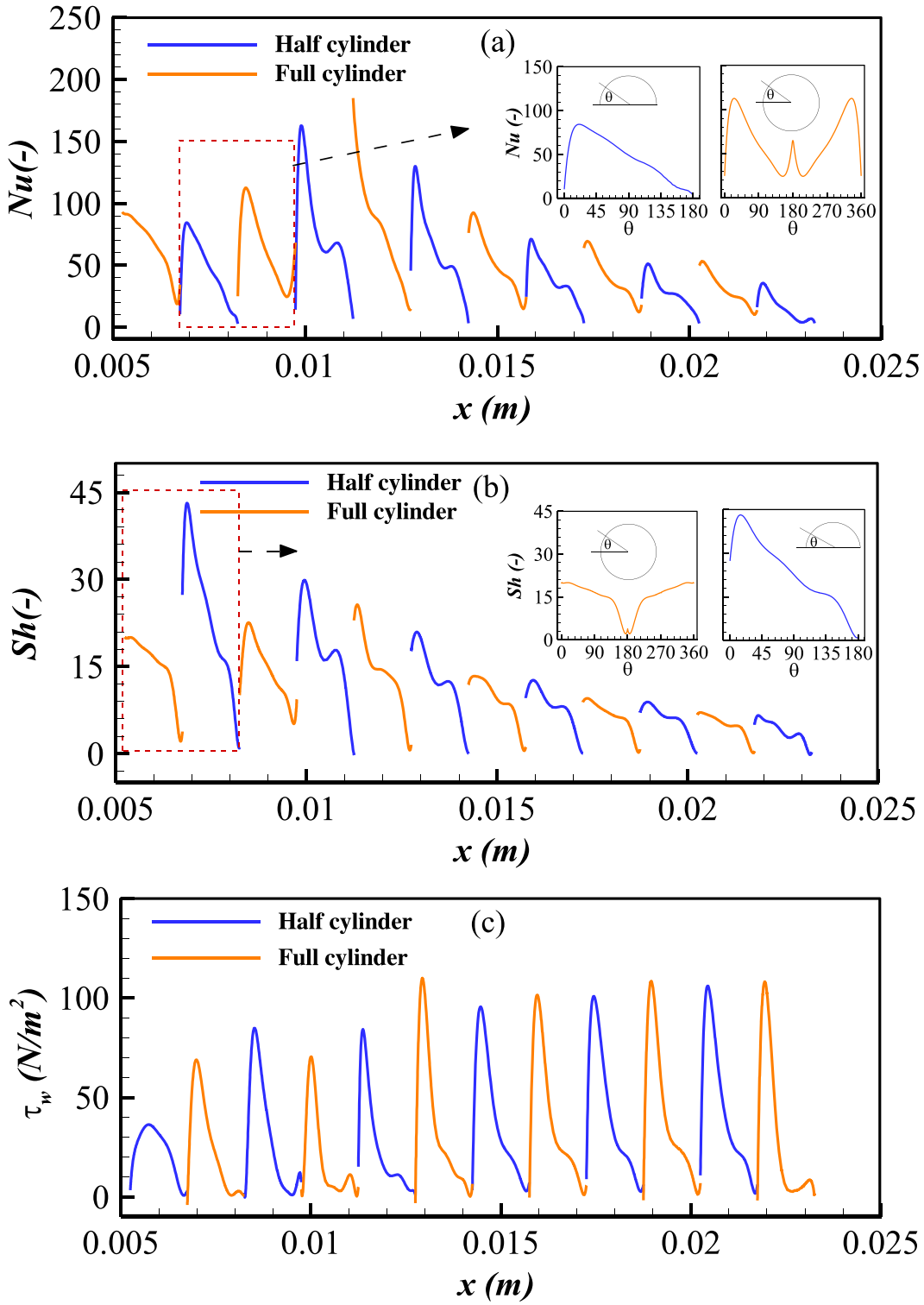

Fig. 13. Case 4 (reacting): local distribution of (a) *Nu*, (b) *Sh* and (c) τ_w on catalytic cylindrical surfaces.

studied for many years. However, the use of staggered cylinders with catalyst coatings in a non-planar reactor to enhance the catalytic performance has not been thoroughly explored prior to this study. The cylinders intensify turbulence, which further improves the mass and heat transfer at the surfaces, leading to an increased fuel conversion. To model turbulence, LES is an attractive option; however, due to its high computational demands, 3D modelling with LES in such reactors has been scarcely explored in the literature. Hence, this paper presents LES modelling in a non-planar reactor to investigate the intensification of the catalytic process. The results demonstrate that the LES model effectively predicts the catalytic reacting flow. A non-planar reactor with cylindrical surfaces coated with catalysts is studied and compared with a planar reactor having the same inner surface coating. The turbulence in the non-planar reactor significantly enhances mass and heat transfer at the catalytic surfaces, thereby intensifying the catalytic process. Under the considered operating conditions in the non-planar reactor, gas-phase combustion is completely inhibited, and the catalytic surface temperatures are comparatively low. Furthermore, H_2 conversion in the non-

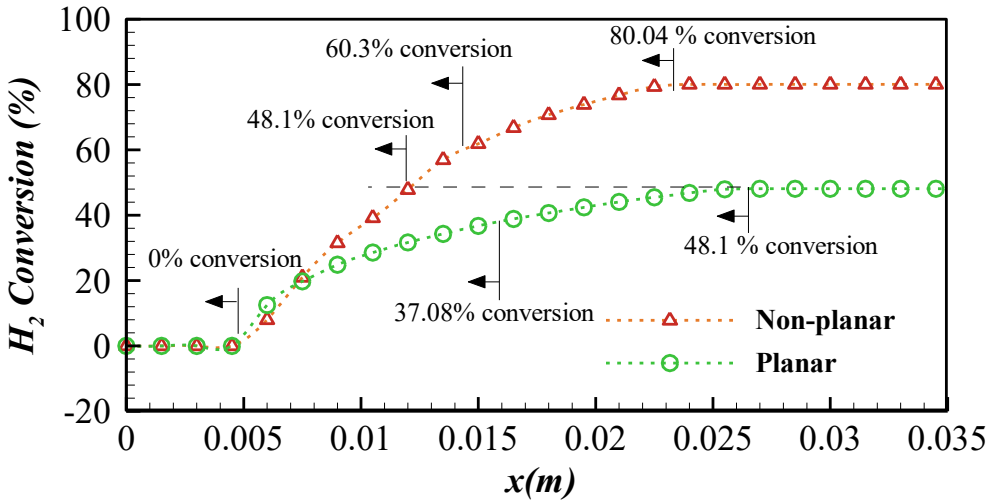

Fig. 14. Hydrogen conversion (%) along the length of the reactor.

planar reactor is significantly higher than in the planar reactor. The increased catalytic activity combined with lower catalytic surface temperatures provides a basis for optimising catalytic reactor design for various applications.

4. Conclusions

The turbulent catalytic combustion of a highly lean, premixed fuel-lean hydrogen/air mixture with an equivalence ratio of 0.15 over a platinum catalyst, at an inflow temperature of 300 K and a Reynolds number of 3500, was investigated. This study examined both the planar and non-planar reactors using large eddy simulation. The numerical method relied on the structured finite volume discretisation, incorporating the turbulent kinetic energy sub-grid model for LES and the eddy dissipation concept for computing species reaction rates. Before analysis, the numerical method underwent validation for both configurations, with experimental results utilised for comparison. The key findings are summarised as follows.

- In the planar catalytic reactor, the flow turbulence remains nearly consistent along the reactor length.
- The non-planar reactor with staggered cylindrical rods significantly increases turbulence, enhancing heat and mass exchange with the catalytic surface and thereby intensifying catalytic combustion.
- In the planar reactor, both *Nu* and *Sh* decrease along the reactor length, while, in non-planar reactor, *Nu* and *Sh* are most effective on both the full and half cylindrical coated surfaces.
- In contrast to the planar reactor, hydrogen conversion in the non-planar reactor is purely catalytic and occurs at lower surface temperatures.
- The non-planar reactor improves H_2 conversion to 80.04 % at the reactor exit, compared to 48.1 % in the planar reactor.
- The non-planar reactor achieves the same output as the planar reactor while using 62.5 % less catalyst.

The non-planar reactor featuring coated staggered cylindrical surfaces shows promise in enhancing the catalytic process and could be significant in the design of catalytic reactors. Upcoming research will explore optimising various design elements, such as reactor geometry, cylinder size and placement, improving flow distribution, and choosing effective catalyst coating techniques.

CRediT authorship contribution statement

Md Nur Alam Mondal: Writing – original draft, Visualization, Validation, Software, Methodology, Investigation, Funding acquisition, Formal analysis, Data curation, Conceptualization. **Nader Karimi:** Writing – review & editing, Supervision, Conceptualization. **S. David Jackson:** Writing – review & editing, Supervision. **Manosh C. Paul:** Writing – review & editing, Supervision, Resources, Project administration, Funding acquisition, Conceptualization.

Declaration of competing interest

The authors declare that they have no known competing financial interests or personal relationships that could have appeared to influence the work reported in this paper.

Data availability

Data will be made available on request.

Acknowledgement

The first author is a Commonwealth Scholar (CSC ID: BDCS-2020-54), funded by the UK government. The computational results were obtained using ARCHIE-WeSt High-Performance Computer (www.archie-west.ac.uk). N. Karimi acknowledges the financial support provided by EPSRC through grant number EP/X019551/1. We thank Dr. John Mantzaras (Paul Scherrer Institut) for sharing useful experimental and numerical data used for validation in this work.

References

[1] Fumey B, Buetler T, Vogt UF. Ultra-low NOx emissions from catalytic hydrogen combustion. Appl Energy 2018;213:334–42. https://doi.org/10.1016/j.apenergy.2018.01.042.
[2] Smith LL, Karim H, Castaldi MJ, Etemad S, Pfefferle WC, Khanna V, et al. Rich-catalytic lean-burn combustion for low-single-digit NOx gas turbines. J Eng Gas Turbine Power 2005;127:27–35. https://doi.org/10.1115/1.1787510.
[3] Mantzaras J. Catalytic combustion of hydrogen, challenges, and opportunities. In: Advances in Chemical Engineering, Academic Press Inc., 2014: pp. 97–157. doi: 10.1016/B978-0-12-800422-7.00003-0.
[4] Appel C, Mantzaras J, Schaeren R, Bombach R, Inauen A, Kaeppeli B, et al. An experimental and numerical investigation of homogeneous ignition in catalytically stabilized combustion of hydrogen/air mixtures over platinum. Combust Flame 2002;128:340–68. https://doi.org/10.1016/S0010-2180(01)00363-7.
[5] Sui R, Mantzaras J, Bombach R, Khatoonabadi M. High-pressure kinetic interactions between CO and H2 during syngas catalytic combustion on PdO. Proc Combust Inst 2023;39:5611–9. https://doi.org/10.1016/j.proci.2022.06.010.
[6] Wu C-Y, Yang SY, Hsu T-C, Chen K-H. Self-ignition and reaction promotion of H2 with CO2/O2 in Pt-Coated γ-Al2O3 bead reactor. Energy 2016;94:524–32. https://doi.org/10.1016/j.energy.2015.11.017.

[7] Merotto L, Dondè R, De Iuliis S. Study of the performance of a catalytic premixed meso-scale burner. Exp Therm Fluid Sci 2016;73:115–21. https://doi.org/10.1016/j.expthermflusci.2015.10.005.

[8] Sui R, Mantzaras J. Combustion stability and hetero-/homogeneous chemistry interactions for fuel-lean hydrogen/air mixtures in platinum-coated microchannels. Combust Flame 2016;173:370–86. https://doi.org/10.1016/j.combustflame.2016.08.011.

[9] Mantzaras J. Progress in non-intrusive laser-based measurements of gas-phase thermoscalars and supporting modelling near catalytic interfaces. Prog Energy Combust Sci 2019;70:169–211. https://doi.org/10.1016/j.pecs.2018.10.005.

[10] Bolaños-Chaverri F, Mantzaras J, Griffin T, Bombach R, Winkler D. An experimental and numerical investigation of the catalytic-rich/gaseous-lean combustion of H2/CO/air mixtures at 8 bar. Proc Combust Inst 2021;38:5443–51. https://doi.org/10.1016/j.proci.2020.06.149.

[11] Mondal MNA, Karimi N, Jackson SD, Paul MC. Numerical investigation of premixed hydrogen/air combustion at lean to ultra-lean conditions and catalytic approach to enhance stability. Int J Hydrogen Energy 2023;48:18100–15. https://doi.org/10.1016/j.ijhydene.2023.01.298.

[12] Chen G-B, Chen C-P, Wu C-Y, Chao Y-C. Effects of catalytic walls on hydrogen/air combustion inside a micro-tube. Appl Catal A Gen 2007;332:89–97. https://doi.org/10.1016/j.apcata.2007.08.011.

[13] Sui R, Prasianakis NI, Mantzaras J, Mallya N, Theile J, Lagrange D, et al. An experimental and numerical investigation of the combustion and heat transfer characteristics of hydrogen-fueled catalytic microreactors. Chem Eng Sci 2016;141:214–30. https://doi.org/10.1016/j.ces.2015.10.034.

[14] Ghermay Y, Mantzaras J, Bombach R, Boulouchos K. Homogeneous combustion of fuel-lean H2/O2/N2 mixtures over platinum at elevated pressures and preheats. Combust Flame 2011;158:1491–506. https://doi.org/10.1016/j.combustflame.2010.12.025.

[15] Kozhukhova AE, du Preez SP, Bessarabov DG. Catalytic hydrogen combustion for domestic and safety applications: a critical review of catalyst materials and technologies. Energies (Basel) 2021;14:4897. https://doi.org/10.3390/en14164897.

[16] Battistella F, Donazzi A, Ravidà A, Valenti G, Groppi G. Numerical modelling and experimental testing of the hydrogen ultra-lean combustion on an adiabatic catalytic monolith in diverse working conditions. Int J Hydrogen Energy 2024;71:1405–15. https://doi.org/10.1016/j.ijhydene.2024.05.262.

[17] Yuan L-J, Zhao Z-C, Wang W-Q, Wang Y-F, Liu Y-J. Review of catalysts, substrates, and fabrication methods in catalytic hydrogen combustion with further challenges and applications. Energy Fuel 2024;38:4881–903. https://doi.org/10.1021/acs.energyfuels.3c04923.

[18] Kim J, Yu J, Lee S, Tahmasebi A, Jeon C-H, Lucas J. Advances in catalytic hydrogen combustion research: catalysts, mechanism, kinetics, and reactor designs. Int J Hydrogen Energy 2021;46:40073–104. https://doi.org/10.1016/j.ijhydene.2021.09.236.

[19] Nauman M, Pan J, Wang Y, Li F, Oluwaleke Ojo A, Raza A. A review of recent advancements in micro combustion techniques to enhance flame stability and fuel residence time. Int J Hydrogen Energy 2024;49:1165–93. https://doi.org/10.1016/j.ijhydene.2023.09.050.

[20] Ghermay Y, Mantzaras J, Bombach R. Effects of hydrogen preconversion on the homogeneous ignition of fuel-lean H2/O2/N2/CO2 mixtures over platinum at moderate pressures. Combust Flame 2010;157:1942–58. https://doi.org/10.1016/j.combustflame.2010.02.016.

[21] Chabane AM, Truffin K, Angelberger C. Direct numerical simulation of catalytic combustion in a meso-scale channel with non-planar walls. Combust Flame 2020;222:85–102. https://doi.org/10.1016/j.combustflame.2020.08.033.

[22] Smith BL, Stepan JJ, McEligot DM. Velocity and pressure measurements along a row of confined cylinders. J Fluids Eng Trans ASME 2007;129:1314–27. https://doi.org/10.1115/1.2776970.

[23] Appel C, Mantzaras J, Schaeren R, Bombach R, Inauen A. Turbulent catalytically stabilized combustion of hydrogen/air mixtures in entry channel flows. Combust Flame 2005;140:70–92. https://doi.org/10.1016/j.combustflame.2004.10.006.

[24] Chao Y-C, Chen G-B, Hsu C-J, Leu T-S, Wu C-Y, Cheng T-S. Operational characteristics of catalytic combustion in a platinum microtube. Combust Sci Technol 2004;176:1755–77. https://doi.org/10.1080/00102200490487599.

[25] Mantzaras J, Appel C, Benz P, Dogwiler U. Numerical modelling of turbulent catalytically stabilized channel flow combustion. Catal Today 2000;59:3–17. https://doi.org/10.1016/S0920-5861(00)00268-6.

[26] Mantzaras J. Understanding and modeling of thermofluidic processes in catalytic combustion. Catal Today 2006;117:394–406. https://doi.org/10.1016/j.cattod.2006.06.047.

[27] Lu Q, Wang Q, Fan B, Zhang Y, Wang Y, Nauman M, et al. Numerical study on hydrogen heterogeneous reaction characteristic in a micro catalytic combustor with blunt body. Fuel 2024;357:129632. https://doi.org/10.1016/j.fuel.2023.129632.

[28] Lucci F, Frouzakis CE, Mantzaras J. Three-dimensional direct numerical simulation of turbulent channel flow catalytic combustion of hydrogen over platinum. Proc Combust Inst 2013;34:2295–302. https://doi.org/10.1016/j.proci.2012.06.110.

[29] Arani BO, Frouzakis CE, Mantzaras J, Boulouchos K. Direct numerical simulations of turbulent catalytic and gas-phase combustion of H2/air over Pt at practically-relevant Reynolds numbers. Proc Combust Inst 2019;37:5489–97. https://doi.org/10.1016/j.proci.2018.05.103.

[30] Arani BO, Frouzakis CE, Mantzaras J, Boulouchos K. Three-dimensional direct numerical simulations of turbulent fuel-lean H2/air hetero-/homogeneous combustion over Pt with detailed chemistry. Proc Combust Inst 2017;36:4355–63. https://doi.org/10.1016/j.proci.2016.05.009.

[31] Ström H, Sasic S. Heat and mass transfer in automotive catalysts—The influence of turbulent velocity fluctuations. Chem Eng Sci 2012;83:128–37. https://doi.org/10.1016/j.ces.2011.10.070.

[32] Bioche K, Bricteux L, Bertolino A, Parente A, Blondeau J. Large Eddy Simulation of rich ammonia/hydrogen/air combustion in a gas turbine burner. Int J Hydrogen Energy 2021;46:39548–62. https://doi.org/10.1016/j.ijhydene.2021.09.164.

[33] Abdel-Raheem MA, Ibrahim SS, Malalasekera W, Masri AR. Large eddy simulation of hydrogen–air premixed flames in a small-scale combustion chamber. Int J Hydrogen Energy 2015;40:3098–109. https://doi.org/10.1016/j.ijhydene.2014.12.042.

[34] Wu C-Y. Numerical modelling of hydrogen catalytic reactions over a circular bluff body. Int J Hydrogen Energy 2022;47:37204–17. https://doi.org/10.1016/j.ijhydene.2021.12.006.

[35] Das K, Basu D, Painter SL, Howard LD, Green ST. Detached eddy simulations and transient rans simulations of turbulent flow in the lower plenum of a gas-cooled reactor. In: Volume 2: Fuel Cycle and High Level Waste Management; Computational Fluid Dynamics, Neutronics Methods and Coupled Codes; Student Paper Competition, ASMEDC, 2008: pp. 411–423. doi: 10.1115/ICONE16-48514.

[36] Brambilla A, Frouzakis CE, Mantzaras J, Tomboulides A, Kerkemeier S, Boulouchos K. Detailed transient numerical simulation of H2/air hetero-/homogeneous combustion in platinum-coated channels with conjugate heat transfer. Combust Flame 2014;161:2692–707. https://doi.org/10.1016/j.combustflame.2014.04.003.

[37] M.E. Coltrin, R.J. Kee, F.M. Rupley, E. Meeks, SURFACE CHEMKIN-III: A Fortran package for analysing heterogeneous chemical kinetics at a solid-surface - gas-phase interface, Report No. SAND-96-8217, Albuquerque, NM, and Livermore, CA (United States), 1996. doi: 10.2172/481906.

[38] Kim W-W, Menon S, Kim W-W, Menon S. Application of the localized dynamic subgrid-scale model to turbulent wall-bounded flows. In: 35th Aerospace Sciences Meeting and Exhibit, American Institute of Aeronautics and Astronautics, Reston, Virigina, 1997. doi: 10.2514/6.1997-210.

[39] Stewart WE. Multicomponent mass transfer. By Ross Taylor and R. Krishna, Wiley, New York, 1993, 579 pp, AIChE Journal 41 (1995) 202–203. doi: 10.1002/aic.690410124.

[40] Merk HJ. The macroscopic equations for simultaneous heat and mass transfer in isotropic, continuous and closed systems. Appl Sci Res 1959;8:73–99. https://doi.org/10.1007/BF00411741.

[41] Germano M, Piomelli U, Moin P, Cabot WH. A dynamic subgrid-scale eddy viscosity model. Phys Fluids A 1991;3:1760–5. https://doi.org/10.1063/1.857955.

[42] Gran IR, Magnussen BF. A numerical study of a bluff-body stabilized diffusion flame. Part 2. Influence of combustion modeling and finite-rate chemistry. Combust Sci Technol 1996;119:191–217. https://doi.org/10.1080/00102209608951999.

[43] Warnatz J, Allendorf MD, Kee RJ, Coltrin ME. A model of elementary chemistry and fluid mechanics in the combustion of hydrogen on platinum surfaces. Combust Flame 1994;96:393–406. https://doi.org/10.1016/0010-2180(94)90107-4.

[44] Deutschmann O, Schmidt R, Behrendt F, Warnat J. Numerical modelling of catalytic ignition. Symp (Int) Combust 1996;26:1747–54. https://doi.org/10.1016/S0082-0784(96)80400-0.

[45] Kee RJ, Rupley FM, Meeks E, Miller JA. CHEMKIN-III: A FORTRAN chemical kinetics package for the analysis of gas-phase chemical and plasma kinetics, Report No. SAND-96-8216, Albuquerque, NM, and Livermore, CA (United States), 1996. doi: 10.2172/481621.

[46] Kee RJ, Dixon-Lewis G, Warnatz J, Coltrin ME, Miller JA. A Fortran computer code package for the evaluation of gas-phase, multicomponent transport properties, Report No. SAND-86-8246, United States, 1986. https://www.osti.gov/biblio/7157265.

[47] He S, He K, Seddighi M. Laminarisation of flow at low Reynolds number due to streamwise body force. J Fluid Mech 2016;809:31–71. https://doi.org/10.1017/jfm.2016.653.

[48] Wardana ING, Ueda T, Mizomoto M. Velocity-temperature correlation in strongly heated channel flow. Exp Fluids 1995;18:454–61. https://doi.org/10.1007/BF00208469.

[49] Kim J, Moin P, Moser R. Turbulence statistics in fully developed channel flow at low Reynolds number. J Fluid Mech 1987;177:133–66. https://doi.org/10.1017/S0022112087000892.

[50] Bae JH, Yoo JY, Choi H, McEligot DM. Effects of large density variation on strongly heated internal air flows. Phys Fluids 2006;18. https://doi.org/10.1063/1.2216988.

[51] Appel C, Mantzaras J, Schaeren R, Bombach R, Kaeppeli B, Inauen A. An experimental and numerical investigation of turbulent catalytically stabilized channel flow combustion of hydrogen/air mixtures over platinum. Proc Combust Inst 2002;29:1031–8. https://doi.org/10.1016/S1540-7489(02)80130-4.